Additive Manufacturing of Bimetallic Structures

Amit Bandyopadhyay*, Yanning Zhang, and Bonny Onuike

W. M. Keck Biomedical Materials Research Lab

School of Mechanical and Materials Engineering

Washington State University

Pullman, WA 99164-2920, USA.

*E-mail: amitband@wsu.edu

Table of Contents

Abstract

Current industrial applications demand materials with customized features and site-specific properties, and many such applications use bimetallic structures. Bimetallic structures offer unique properties from both materials. Bimetallic materials are made by joining two different materials via welding or brazing. Although welding techniques to join two metallic materials are economical, there are still many critical issues, such as managing the heat-affected zone, cracking, and premature failures due to brittle intermetallic phase formation, especially for joining two dissimilar metals, and reproducibility. In recent years, metal additive manufacturing (AM) has been explored towards processing bimetallic materials. Metal AM systems are designed with multiple feedstock materials, enabling various printing strategies to process bimetallic structures. This review aims to aid researchers in understanding AM processing of bimetallic structures. Various processing strategies, characterization methods, challenges, and future directions are discussed. We envision that this review will help further the implementation of AM technologies in bimetallic structures.

Keywords: Additive manufacturing; Bimetallic structures; Metals; Joining.

1.0 Introduction

The motivation for developing different alloys was to exceed the performance limitations of pure metals in engineering applications. **Fig.1** shows a broad outline of processing metals and alloys for different applications. Conventional alloying, a revolutionary innovation, could create a new metallic material by mixing two or more metals or non-metals in a molten state. Alloys

can offer improved properties such as higher toughness, higher strength, better wear, and corrosion resistance than pure metals. Over the last few centuries, different alloys have been developed, such as numerous steels (such as stainless steels), Cu-based alloys (Bronze), Ni-based superalloys (Inconel), several titanium alloys (Ti6Al4V), and widely implemented for various industrial applications. Today's hi-tech engineering applications demand metallic materials with enhanced but customized and sometimes site-specific properties that a single composition could not satisfy. Bimetallic structures, a combination of two different metals, can be manufactured by joining, such as welding or brazing those alloys. Bimetallic structures could solve a single material's limitations while maintaining each material's desired properties in one structure. These advantages could lead to unique properties common in most engineering applications by joining different metallic materials to form various bimetallic structures. Therefore, it is very confident that bimetallic materials could resolve material selection issues in current industrial applications and customize material properties based on applications' performance demands.

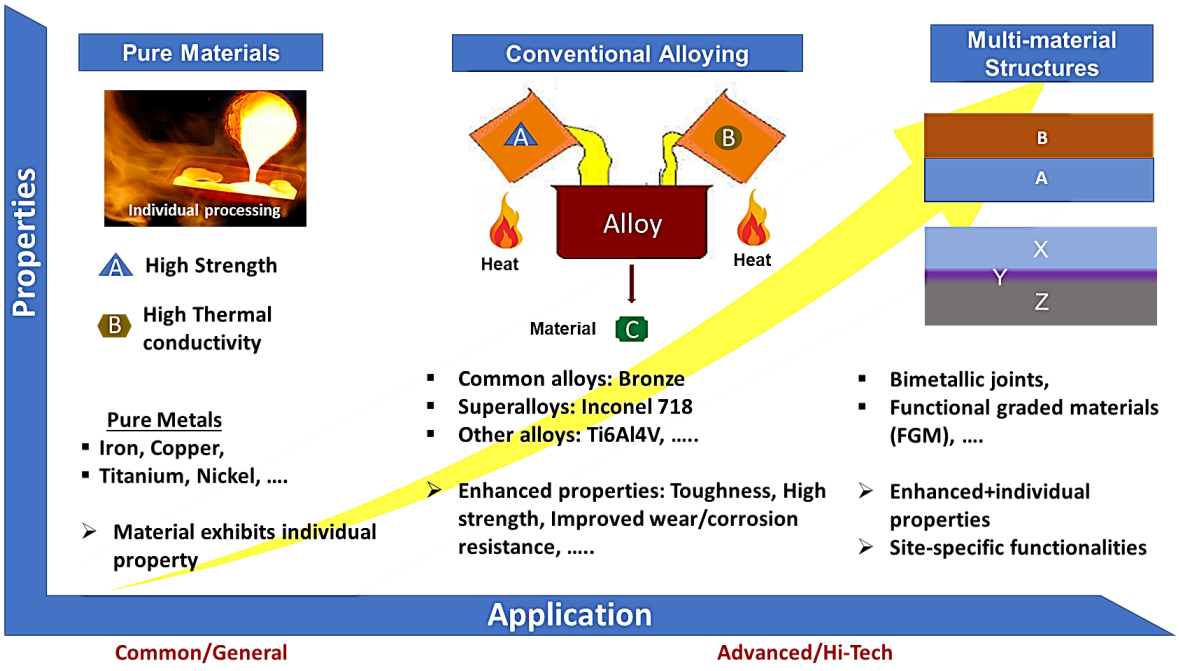

Figure 1. Processing of metals and alloy.

A bimetallic structure could be processed using conventional or additive manufacturing (AM) methods, as shown in **Fig. 2.** Welding and brazing techniques are probably the most commonly used conventional methods for joining two different metallic materials. Different

welding techniques such as arc welding, explosion welding, laser butt welding, and friction stir welding can be applied for joining [1–9]. Although welding techniques to join two metallic materials is economical, there are still some critical issues for bimetallic structures, such as leading a sizeable heat-affected zone (HAZ) at the joint and cracking due to brittle intermetallic phase formation, especially for joining two dissimilar metals. Brazing, a liquid–solid-state bonding process, is performed at a lower temperature than welding. This process is used with filler (braze) metal to join wide varieties of dissimilar metals with improved bonding strength. Diffusion bonding is increasingly used to join difficult-to-bond combinations of materials, such as immiscible dissimilar metals, metals to ceramics combinations, by applying pressure and heat at joining surfaces where the strength of the diffusion-bonded joint is a function of plastic deformation.

Using metal AM to fabricate customized objects is currently the trend in many industries. Current metal AM technologies such as directed energy deposition (DED): blown-powder or wire-feed processes can build parts in single or multiple compositions. Powder-bed fusion is gaining attention to processing multi-material structures, as well. Because AM is layer-by-layer processing, various strategies could be applied to build a bimetallic structure by taking this advantage. Direct deposition strategy is simply depositing one metallic material on top of another. This strategy is suitable for fabricating a bimetallic structure with 'similar' metal characteristics, which means the two metallic materials have similar thermal properties and show good solid solubility. The bimetallic structure fabricated by direct deposition may have a sharp transition from metals A to B. However, this sharp transition may cause some defects at an elevated temperature environment due to the mismatch of metallic materials' thermal properties. Instead of having a sharp transition, applying a compositional gradation at the interface could create a smooth transition between the two metallic materials, reducing the adverse effects caused by the sharp transition. The compositional gradation creates a graded transition at the interface between the two metallic materials, and this bimetallic material can also be seen as functionally graded material (FGM). Both direct deposition and compositional gradation strategies do not require a third material to serve as a bonding material. The introduction of compatible third bonding material is commonly used for joining two dissimilar metals to increase the bond strength of the two metals. This third material can be a single composition (intermediate bond layer) or a mixed composition (compositional bond layer). A third metallic

material selected as an intermediate bond layer works like the welding process's filler material. The selected material should be able to bond both metals with good strength. The compositional bond layer borrows the compositional gradation strategy and adds a third material into the graded transition. The added material is not limited to metallic materials; in some cases, ceramic materials could also enhance the bond strength [10–16]. Although some welding techniques can join dissimilar metals, using metal AM technologies to fabricate bimetallic structures gives more precise control, especially at the transition region, and fabricates parts with complex shapes. The AM methods and bimetallic materials processing strategies are discussed later.

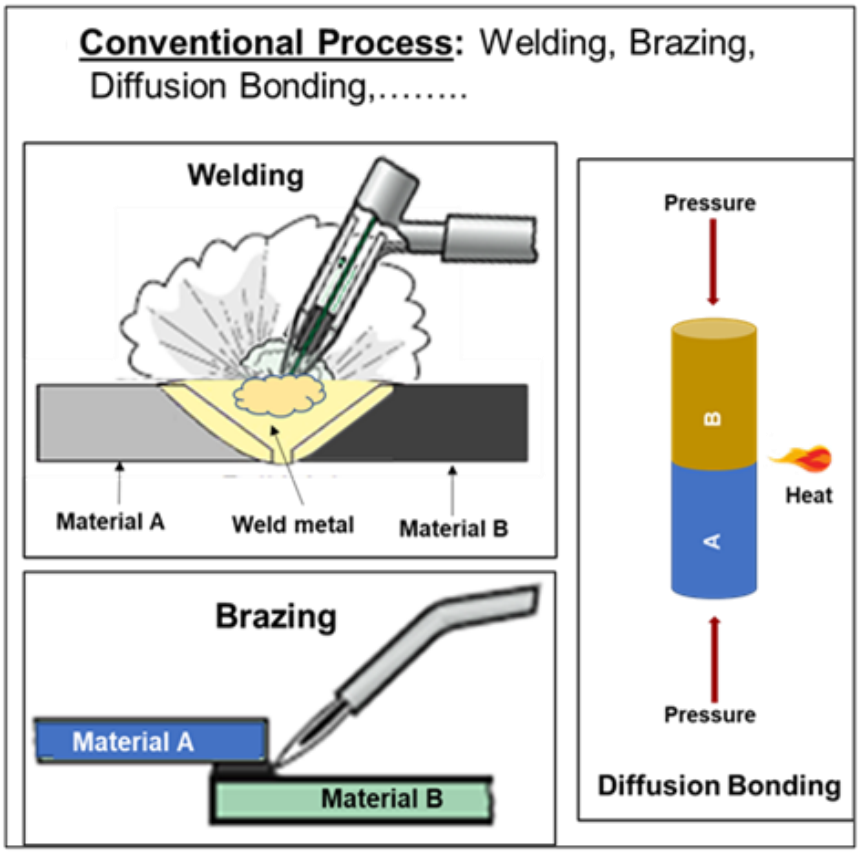

Figure 2. Conventional manufacturing methods bimetallic structures.

Although current metal AM technologies have many advantages in processing bimetallic structures, some critical issues and challenges need to be addressed. Specifically, AM is a layer-by-layer fabrication process based on a digital file that gives high customization flexibility on a part's design. Additionally, current AM systems for metallic materials can control the processing

parameters such as the feedstock feed rate, energy input, and scan speed, allowing users to adjust and optimize the processing parameters based on printing results. Moreover, the configuration of today's metal AM systems, especially the directed energy deposition (DED) systems, is updated with multiple feeders for the feedstock(s), making it both possible and easier to manufacture bimetallic structures. Despite the advantages, some challenges are there due to materials' properties (e.g., metallurgical incompatibility), the user's choice of processing parameters for each material, and transition strategies during printing material B on material A. For example, the optimized processing parameters for a pure metal A may not be optimal for making a bimetallic structure that contains metal A and metal B, and the choice of processing parameters could also have a significant impact on the properties (e.g., secondary phase formation, microstructures, and properties) of the final bimetallic structure. Furthermore, most reported AM-made bimetallic structures are still in the research stage, which means the samples' size and shape are still limited to simple geometries such as cylinders and blocks. As discussed in the next section, the successful development of bimetallic samples has gained various industrial applications. Although these AM-made bimetallic samples may have remarkable properties, it is questionable whether the same compositions can retain the properties on a larger scale or for more complex geometries to survive in an actual application. To this end, a comprehensive review is necessary to document recent advances in processing bimetallic structures via metal AM.

This review aims to aid materials and manufacturing engineers and researchers who do not understand bimetallic AM processing, and those who understand AM but could benefit from utilizing bimetallic processing. The key difference between previous reviews and the current work is detailed descriptions of works that includes but is not limited to metal functionally graded materials, which have been extensively reviewed [17–21]. Further, we detail various processing strategies and challenges, characterization methods for these structures, physical properties, and future directions. It is important to note that modeling and simulation are also crucial for any metal AM process; however, this review does not cover advancements in modeling and simulation related to bimetallic structures. We envision that this review will aid current AM processing for bimetallic materials by providing the insights and perspectives necessary for the full-scale implementation of bimetallic metal AM technologies.

2.0 Applications of bimetallic structures

Applications of bimetallic structures can cover many fields such as automobile, aerospace, energy, nuclear, transportation, and medical [22–31]. **Fig. 3** demonstrates some images of bimetallic materials applied in today's industrial applications. Bimetallic materials have been proposed in body frames, engine blocks, and pistons to reduce the deadweight in automobiles. Additionally, using Fe/Al bimetallic as a cylinder's wall in the engine could increase the heat conductivity and corrosion resistance (**Fig. 3a)** [32]. Researchers have successfully fabricated a laser additive manufacturing (LAM) processed Ti6Al4V/$Ti_48Al_2Cr_2Nb$ (TC4/TiAl) bimetallic structure via vanadium interlayer, which could potentially be used as integral turbine blade discs for aero-engines (**Fig. 3b)** [33]. Aerospace industries have widely adopted metal AM technologies since the advantages such as the capability of fabricating complex shapes and reducing time and cost were recognized. NASA has used metal AM technologies to fabricate bimetallic as channel wall nozzle, enabling more flexibility on design and overcoming challenges such as materials' selection for the high-temperature environment, manufacturing methods of large parts with tight tolerances complex features manufacturing with high efficiency [34]. **Fig. 3c** to **3f** show the images of metal AM processed bimetallic nozzles from NASA. The blown powder DED technique fabricates a nozzle manifold with a bimetallic structure in **Fig. 3c**. NASA also developed the laser wire direct closeout (LWDC) method (**Fig. 3d**), dedicating explicitly to channel closeout manufacturing with monolithic and bimetallic materials. Although monolithic materials are mainly used for channel wall manufacturing, some engine applications still demand a bimetallic design solution with a copper liner for a higher heat flux environment [34]. A bimetallic nozzle structure implemented with copper liner with radial and axial compositional gradation could minimize weight and enhance thermal and structural margins [34–36]. Stainless-based or Ni-based superalloy combined with copper alloys bimetallic is primarily selected for nozzle structure fabrication [34,37]. **Fig. 3e** shows the cross-section of an LWDC processed bimetallic intergraded channel closeout. A continuous and repeatable bond between the ribs and the base materials ensures structural strength [34]. Explosive welding

(EXW) is a solid-state joining method for similar and dissimilar materials bonding [38–42]. **Fig. 3f** shows an example of an EXW processed bimetallic axial liner on a nozzle structure [34].

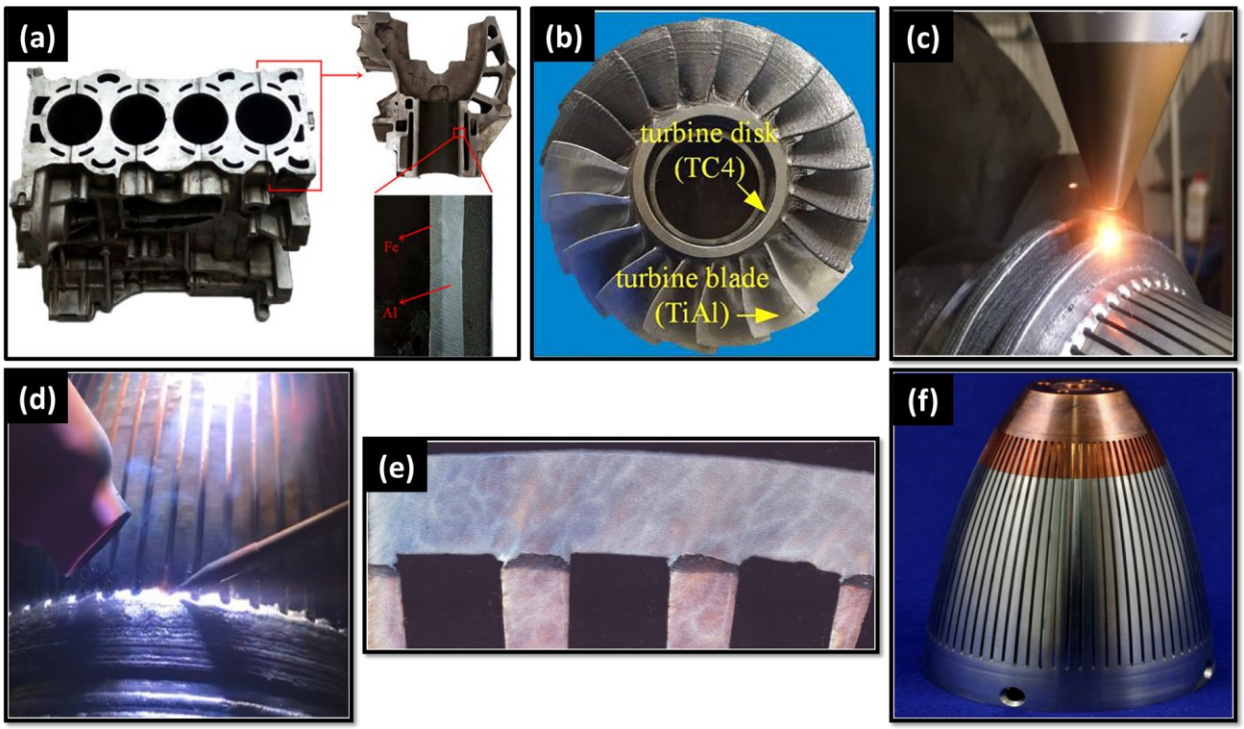

Figure 3. (a) An engine block with four cylinders and the micro image of the cross-section of a cylinder wall (Fe/Al bimetallic) [32]. (b) Schematic showing the laser additive manufacturing (LAM) processed Ti6Al4V/$Ti_48Al_2Cr_2Nb$ (TC4/TiAl) bimetallic aero-engine turbine blade [33]. (c) DED process implementing nozzle manifold preparations [34]. (d) Bimetallic nozzle closeout processed by laser wire direct closeout (LWDC) technique [34]. (e) Image of the cross-section of LWDC prepared bimetallic channel wall nozzle [34]. (f) Explosive welding processed axial bimetallic liner on nozzle [34].

Many scientific papers have been published in recent years, focusing on various bimetallic structures to meet those challenging needs discussed throughout the manuscript [12–14,30,43–51]. These examples show compatible and non-compatible materials joined by simple direct bonding or various creative routes. Inconel 718 was used for bimetallic structures with GRCop84 to improve thermal conductivity [50], while CoCrMo was joined with Ti to minimize metal ion release in the body during articulation [30]. For structural application, bimetallic structures of Ti with Inconel 718 [13] or Al12Si [49], or Al_2O_3 [12] were also demonstrated

using the directed energy deposition process. The following sections elaborate on innovations in processing science, various characterization approaches, and their applications.

3.0 Current AM technologies for manufacturing bimetallic structures

This section discusses current laser-based metal AM technologies for processing bimetallic structures and related challenges. **Table 1** summarizes some of the advantages and disadvantages of these AM technologies.

3.1 Bimetallic structures using powder-based directed energy deposition (DED)

Powder-based directed energy deposition (DED) is a metal AM technology that uses a focused laser as energy input and metal powder as feedstock materials (**Fig. 4a**). The metal powders are fed through the powder feed line by a carrier gas, typically argon, to the laser's focal point. Based on the toolpath design, the working stage moves in X and Y directions in a raster scanning fashion. The fed powders melt at the laser focal point and create a molten metal pool. The molten pool experiences rapid solidification during the raster scanning motion and forms a deposited line. Once the first layer is entirely deposited, the laser head moves up in the Z direction and repeats the powder-deposition process on top of the previous layer until the part geometry is complete. The entire work chamber is sealed and usually filled with inert gas during laser processing, or the melt pool is shielded around to prevent oxidation. An O_2 sensor is commonly installed inside the work chamber to monitor the oxygen level. Processing parameters such as laser power, powder feed rate, and scan speed can be adjusted anytime during the processing. Dual or multiple powder feeders allow bimetallic/multi-materials additive manufacturing in a single process. The powder feed rate of each powder feeder could be adjusted individually during the AM fabrication, applying different fabrication strategies. DED systems can also have a five-axis or free-axis deposition head or work stage, and co-axial powder deposition features allow laser deposition on a non-flat surface and improve the powder deposition efficiency [46].

Many bimetallic structures have been successfully developed using the power DED technology. Imran et al. utilized the DED technique to process Cu/H13 tool steel parts [47]. Cu/H13 bimetallic systems were processed by both direct deposition and intermediate bond strategies. Additionally, 41C stainless steel was used as a bonding material. The interfaces of the

as-fabricated samples showed porous and crack-free transition. Cu/H13 bimetallic processed by direct deposition showed higher bond strength of 673 MPa than 41C SS buffered Cu/H13 bimetallic structure of 579 MPa. Ductile dimple fracture behavior was observed in both samples after the tensile tests. The Charpy impact energy of Cu/H13 and 41C SS buffered Cu/H13 was 67.12 J and 67.8 J, respectively. Furthermore, the directly bonded Cu/H13 bimetallic showed higher fracture toughness of 162.3 $MPa/m^{1/2}$ than 41C SS buffered Cu/H13 bimetallic of 152.5 $MPa/m^{1/2}$. Ji et al. [48] fabricated a Ti6Al4V/Inconel 718 bimetallic FGM with the DED technique of 10%, 20%, and 30% Inconel 718 gradient transition layer. The interfaces showed defects-free transition, and the microstructures evolved from columnar to equiaxed grains with Inconel 718. Moreover, intermetallic phases were formed with the increase of Inconel 718, and the phase transformation followed the sequence as $\alpha + \beta \rightarrow \alpha + \beta + Ti_2Ni \rightarrow \beta + TiNi \rightarrow \gamma$ +Laves. The γ +Laves section had the highest microhardness of 1030 HV_1 due to solid solution strengthening and precipitation hardening. DED processing strategies have also been used to fabricate other bimetallic systems such as Ti6Al4V/SS410, Inconel 718/Ti6Al4V, Inconel 718/GRCop84 copper alloy, Ti6Al4V/Al12Si, SS 316L/Al12Si, Al/W, and Cu/Steel [13,43–45,49–54].

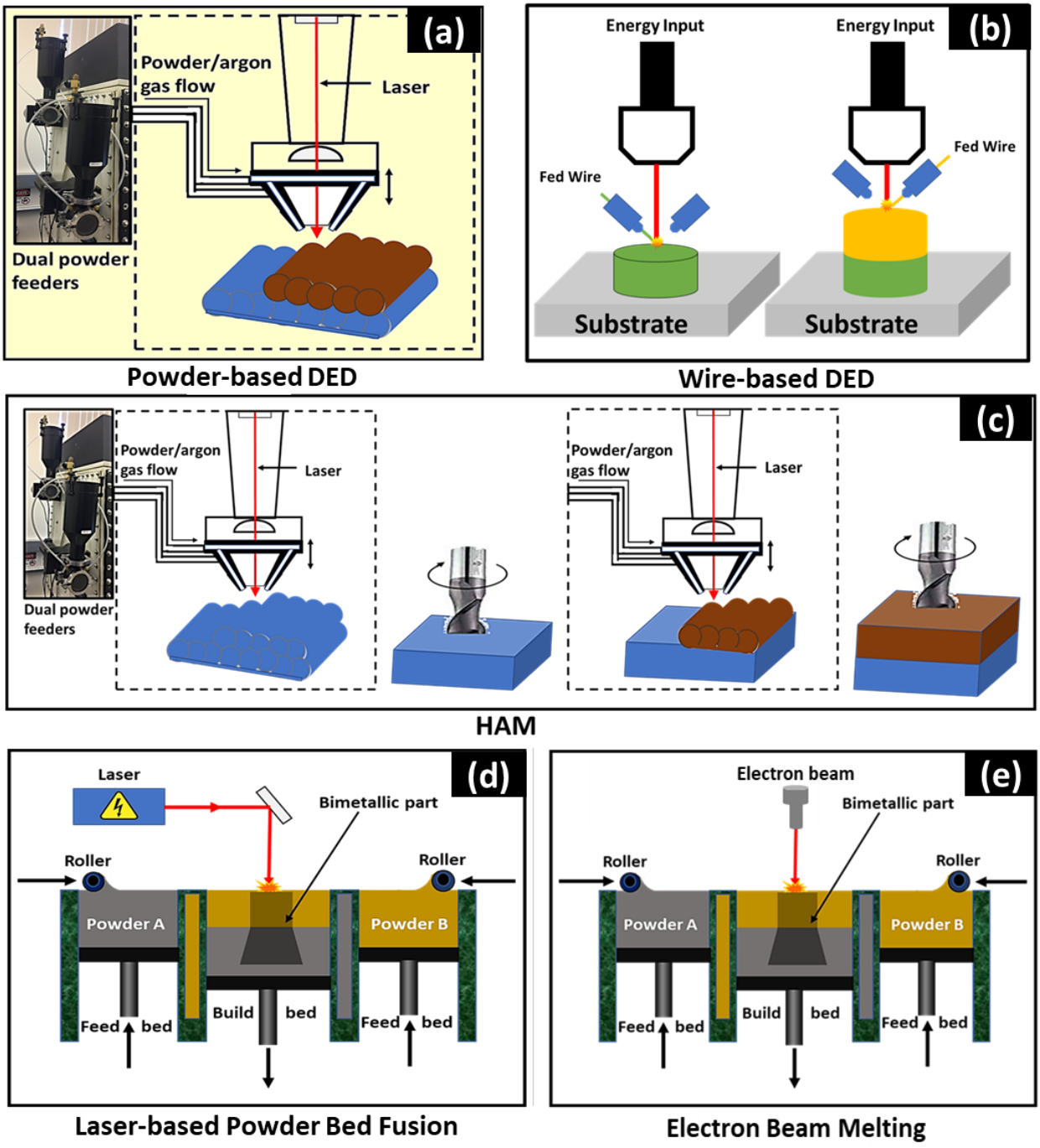

Figure 4. Bimetallic Processing Schematics: (a) Powder-based DED (b) wire-based DED (c) hybrid AM (HAM) (d) laser-based powder bed fusion (e) electron beam melting.

3.2 Wire-based additive manufacturing of bimetallic structures

The wire-based metal AM technology is also a type of DED processing using metallic wires as feedstock instead of powders. The energy source for wire-based AM could be a laser, electron beam, or an electric/plasma arc. Different wire-based metal AM technologies such as wire arc additive manufacturing (WAAM), wire and laser additive manufacturing (WLAM), electron beam freeform fabrication (EBF) have been developed based on different energy sources. The WAAM and WLAM technologies are the most commonly used wire-based AM methods. The EBF processing requires a vacuum working chamber, and the products fabricated by EBF generally have excellent dimensional tolerances. However, some disadvantages include low deposition rate, high cost, and size limitation of the EBF process [55]. The latest wire-based AM systems equip dual wire feeders, allowing for bimetallic structures in one run, **Fig. 4b**.

Wang et al. [56] used the *in situ* dual WAAM method to fabricate NiTi coating on a Ti6Al4V substrate. Pure Ni and pure Ti wires were loaded into each wire feeder. Both Ni and Ti wires were fed to the molten pool simultaneously to perform *in situ* mixing. Argon shield gas was applied to prevent oxidation during the AM processing. Three different arc currents (50 A, 60 A, and 70 A) were utilized to investigate variable energy input effects on the NiTi coating. The results showed that dense and defects free NiTi coatings were deposited on Ti6Al4V substrate. The coating thickness increased from 1.56 mm to 1.91 mm as the arc current rose from 50 A to 70 A due to a higher dilution rate. Microstructural characterization showed that $NiTi_2$ matrix with minor coarse NiTi dendrites was found in the NiTi coating processed with 50 A. Only $NiTi_2$ matrix with α-Ti fine dendrites was obtained in the NiTi coatings processed with 60 A and 70 A. The NiTi coatings' microhardness values processed with 50 A, 60 A, and 70 A were 715 $HV_{0.2}$, 818 $HV_{0.2}$, and 758 $HV_{0.2}$. The intermetallic phase formation, composition, and secondary phase size affected these coatings' microhardness values. Furthermore, wear tests revealed that NiTi coatings significantly increased wear resistance than the Ti6Al4V substrate. Abe et al. demonstrated stainless steel/nickel dissimilar bimetallic system fabricated by the WAAM technique [57]. The stainless steel YS308L was initially deposited on a SS 304 substrate, and then Ni 6082 weld bead was fabricated on top of the YS308L. The interface of the SS/Ni bimetallic showed no welding defects. Based on the microstructural characterization, Austenite and δ-ferrite were found in the WAAM processed stainless steel YS308L section. Ni-based dendritic microstructures were also obtained in the WAAM processed Ni 6082 section.

The microstructure at the interface showed a sharp transition from equiaxed to dendritic. Based on the tensile test results, the WAAM processed SS/Ni bimetallic had comparable tensile strength to SUS304L and Inconel 600 rolled material, indicating sufficient bond strength for use as a mechanical product. A similar study also reported that a WAAM processed steel/nickel bimetallic structural component had an average tensile strength of 634 MPa, higher than the bulk SS and nickel alloy [58]. The higher strength was caused by forming the inter-locking microstructure at the interface and solid solution strengthening. WAAM processed austenitic SS/Inconel 625, low-carbon steel/austenitic SS, nickel aluminum bronze/SS, and AA7075/AA5356 bimetallic systems were also reported [58–61].

3.3 Bimetallic structures using hybrid additive manufacturing (HAM)

The utilization of metal AM in critical applications is generally limited by attainable dimensional accuracy, uniformity of materials properties, and surface quality. Most of the time, the AM fabricated products require post-processing, including heat-treatment and machining, to relieve residual stresses and improve the surface finishing. The concept of hybrid additive manufacturing (HAM) combines machining or subtractive technique with AM technologies into one system. HAM could be a potential solution to high-end product manufacturing with tight tolerance and geometrical challenges. Additionally, combining two processes could help reduce material wastage and cost [62]. **Fig. 4c** demonstrates a HAM method combining the milling with powder DED technique. Once the DED processing completely deposits the layer, the milling head could flatten the deposited layer to decrease defects and improve the bonding between the current layer and the layer to be deposited, consequently improving the part's quality. Other types of HAM, such as CNC machining with arc-based DED technique and selective laser erosion (SLE) with SLM, have been developed and studied [63–65].

Li et al. [66] fabricated an Inconel/steel bimetallic structure via hybrid powder DED and thermal milling system. Initially, the IN718 powder was deposited on a 1040 steel substrate, and then a thermal milling process was performed before the DED part was cooled. This step could avoid preheating for the DED deposition. After the thermal milling process was finished, the SS 316L powder was deposited on the IN718 section. Another milling process was also performed after the SS 316L was entirely deposited. By repeating these steps, the final fabricated object was composed of four sections which were $IN718_1$, SS $316L_1$, $IN718_2$, and SS $316L_2$. Based on the

interfacial characterization result, the interface between $IN718_1$ and SS $316L_1$ showed a clear boundary with no diffusion layer. However, a diffusion layer was obtained at the interface between SS $316L_1$ and $IN718_2$. Columnar dendrites were seen at the diffusion layer and grown towards the heat source. According to the EDS mapping, no element segregation was found in SS 316L sections. An extensive Nb segregation and a small amount of Ti precipitated were found in the DED fabricated IN718 section. The tensile test results showed that the fabricated Inconel/steel bimetallic had a UTS of 516 MPa, lower than the UTS of bulk SS316L (649 MPa) and Inconel 718 (770 MPa). The reduction of the tensile strength was caused by the brittle intermetallic phase, Laves phase, formation.

Yin et al. [67] reported a study of Al/Ti6Al4V bimetallic system fabricated by a HAM with SLM and cold spraying (CS). The SLM technique was first utilized to fabricate the Ti6Al4V section. After the Ti6Al4V section was finished, a heat treatment at 700 ℃ was applied for 1 hour to relieve the residual stresses. Surface finishing was also performed on the SLM-made Ti6Al4V after the heat treatment. Then, Al powder was deposited on the SLM processed Ti6Al4V via CS processing to achieve Al/Ti6Al4V bimetallic. No visible cracks were found at the cross-sectional image of the HAM made Al/Ti6Al4V, which indicated good cohesive strength between the two materials. The phase analysis results showed no intermetallic phases formed at the Al/Ti6Al4V bimetallic interface.

3.4 Bimetallic structures using powder-bed fusion (PBF)

The powder-bed fusion (PBF)-based metal AM technologies include selective laser melting (SLM) that use a laser or an electron beam as an energy source to melt the metallic powders at the build bed [68,69]. The roller feeds a thin layer of metallic powder from the elevated feed bed to the build bed then forms a powder bed. The laser or electron beam [70,71] scans and melts the powder at the selected area based on the part file's tool path. Once a layer is completely formed, the build bed is lowered, and another layer of powder is fed on top of the previous layer. The object's geometry is finally achieved by repeating the layer-by-layer deposition. Like the DED technique, the entire work chamber is filled with inert gas to prevent oxidation during processing. A standard PBF system typically only has one powder feed bed, which requires powder changing for bimetallic part fabrication. Recently developed PBF systems have configurations such as dual powder feed beds (**Figs. 4d and e**) or dual powder feed tanks

that simplify multi-materials part fabrication into one single process [72]. Other research results, including simulation of melt pool behavior/characteristics at mesoscale for IN718/Cu10Sn functionally gradient materials, the morphology of interfacial microstructures of Inconel 718-316L austenitic stainless steel dissimilar alloys, and *in situ* alloying of multi-metals processed via laser PBF, have been reported [73-75].

In a maraging steel/H13 bimetallic structures fabricated using PBF technique [76], two different treatment conditions were applied on the as-fabricated bimetallic: (i) aging treatment (480 ℃ for 6h then air-cooled) and (ii) solution treatment (preheat at 815 ℃ → rapid heating to 982 ℃ for 1h → air-cooled). A comparison study was carried out on the as-fabricated maraging steel/H13, aged maraging steel/H13, and solution-treated maraging steel/H13 bimetallic materials. SEM images showed equiaxed coarse grains with a high density of precipitates found at both as-fabricated and aged maraging steel/H13 bimetallic interfaces. The morphology at the interface of solution treated maraging steel/H13 bimetallic showed lath martensites microstructures. Additionally, the microstructure of the H13 substrate also experienced a martensitic transformation from equiaxed grains. The nanoindentation mapping demonstrated a significant hardness difference between the H13 substrate (~100 HV) and maraging steel sections (~800 HV) in both as-fabricated and aged maraging steel/H13 bimetallic samples. A uniformed hardness distribution was obtained at the solution-treated maraging steel/H13 bimetallic interface, ~ 600 HV. Based on the uniaxial tensile test results of maraging steel/H13 bimetallic samples, the solution-treated bimetallic sample had the highest ultimate tensile strength of 1865.6 MPa than the as-fabricated of 664.2 MPa and aged of 666.1 MPa. The martensitic transformation in the solution-treated bimetallic samples contributed to enhancing the mechanical properties. Another study reported that the SLM technique fabricated an AlSi10Mg/AlCuFeMg bimetallic material [77]. The $AlSi_{10}Mg$ powder was directly deposited on the AlCuFeMg cast alloy substrate with a laser power of 370 W, a scan speed of 1300 mm/s, and a layer thickness of 30 μm. The results showed that large equiaxed grains were observed in the cast alloy substrate and fine cellular structures with an average grain size of 540 nm were found in SLM processed $AlSi_{10}Mg$ section due to the rapid cooling rates. The elemental distribution results demonstrated that the $AlSi_{10}Mg$ and AlCuFeMg coexisted in the first couple of layers due to the dilution effect. Moreover, the interface microstructures showed bimodal grains, indicating a complex metallurgical phenomenon in this region. Other bimetallic systems include SS

316L/$CuSn_{10}$, CuSn/18Ni300, $AlSi_{10}Mg$/C18400 copper alloy, SS 316L/Inconel 718, W-Cu functionally graded material, and Ti-alloy-SS via a Cu-alloy interlayer were also successfully processed via the PBF techniques [78–83].

Table 1. Advantages and disadvantages of AM technologies for bimetallic structure processing

Process Methods	Advantages	Disadvantages	Ref.
Powder-based Directed Energy Deposition: DED, DLD, DMD, LMD, LENS...	• High functionality and integrated features • Moderate processing speed • Functionally graded material generation • On-the-fly processing flexibility • Repair capability	• Requires support structure • Post-processing is usually required. • Powder handling and environmental/safety impact • Mixed powder recycling complexity	[14,22,46], [84 - 87]
Wire-based Directed Energy Deposition: EBF/EBM, LMWD, WAAM...	• Large scale component manufacturing capability • Less material wastage • Low material cost: Feed wire is significantly less expensive compared to metal powder • Easy material handleability and safety.	• High input energy/thermal control • Low resolution • Low deposition rate. • Requires support structure • Needs high material ductility • Post-processing required. • Residual stress/distortions	[14,55,58], [61,88]
Powder-Bed Fusion (PBF): SLM, SLS	• High resolution/accuracy and fine details • Requires no support structure • Fully dense parts • High specific strength and stiffness	• Low build rate • More material wastage • large size limitation • Powder handling and environmental/safety impact • Mixed powder recycling complexity	[75,76], [89 - 91]
Hybrid Additive Manufacturing (HAM)	• High dimensional accuracy • Uniformity of materials properties • High-quality surface finish. • Complex end-use geometries • Reduced material wastage and cost	• Not suitable with in-situ powder bed fusion process • Higher level of automation for manufacturing sequences • Materials machinability and special clamping • Coolant management and cleanness during machining	[14,91- 94]

4.0 Processing strategies

Bimetallic structure manufacturing, especially immiscible dissimilar metals, has experienced bonding issues due to a significant mismatch in base metals' properties. Understanding processing strategies is crucial for manufacturing bimetallic structures from the preceding discussion. **Fig. 5** shows different build/bonding strategies like direct (bonding) deposition, compositional layer, and intermediate bond layer, including compositional bond layer used to manufacture different bimetallic structures. Each approach is dependent on the compatibility of the base materials and how to improve the joint's interfacial property. The overall concept also reveals how to mitigate inherent issues like cracking/delamination, including debonding features associated with dissimilar metals bonding.

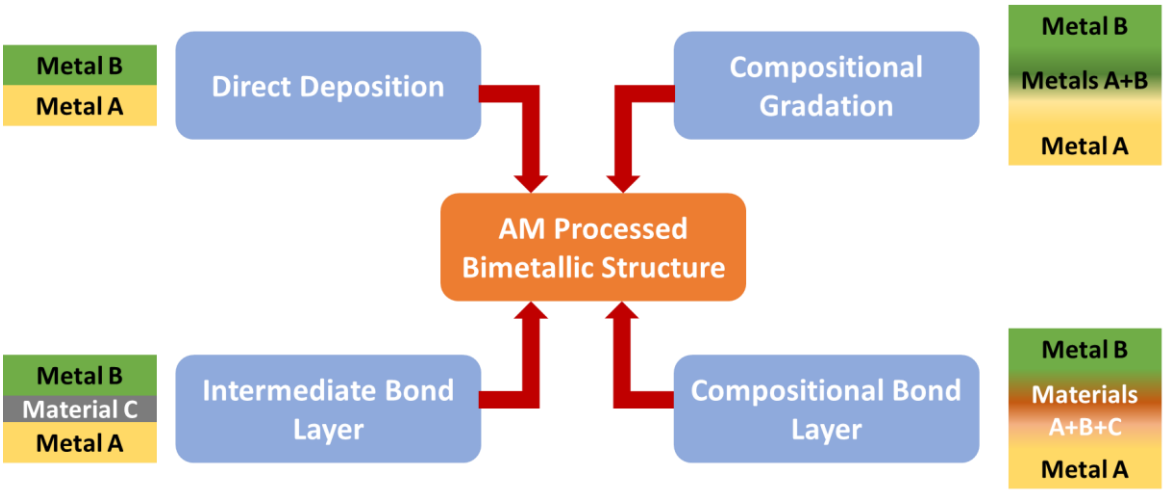

Figure 5. Bimetallic structure processing strategies.

4.1 Direct bonding

Typical methods to fabricate a bimetallic structure are direct bonding/deposition of one material over the other solely due to the strategy's ease and cost-effectiveness. To manufacture a mechanically reliable joint via a direct bonding process requires that the two materials be metallurgically compatible with forming a single-phase solid solution at the joining region and promote good interfacial bond strength. However, as the thermal properties, especially the CTE of materials, play a crucial role during processing, the difference between the CTE of the base

materials should be small to reduce thermally induced stresses responsible for crack initiations and failures at the interface.

Fig. 6 shows different bimetallic structures processed via direct joining by conventional and AM methods. For conventional processes, **Figs 6a and b** show bimetallic structures of titanium alloy/stainless steel materials fabricated via laser butt welding and diffusion bonding processes, respectively [95,96]. These joints showed critical bonding issues due to titanium and stainless steel incompatibility. However, niobium alloy (C103)/nimonic alloy (C263) joint produced through explosive cladding technique [97] showed good bonding at the interface **Fig. 6c**. The direct deposition approach has been widely used through AM processes to fabricate bimetallic joints of compatible dissimilar metals. For instance, GRCop-84 was directly deposited on Inconel 718 material via the LENS process [43], **Fig 6d.** The base materials are metallurgically compatible since Ni-Cu, the base alloy's main constituent element, is an isomorphous alloy system that exhibits complete solubility. The Inconel 718/GRCop-84 bimetallic structure showed good interfacial bond strength. However, an alloy system like Al-Cu that exhibits complex binary phases coupled with the base materials' low laser absorptivity is challenging to process into the bimetallic joint using the laser metal deposition (LMD) methods. Although Zhang et al. [98] investigated the feasibility of fabricating such joint using the friction stir welding method, the bond strength was low, as shown in **Fig. 6e**.

Ideally, the direct bonding approach is unsuitable for joining dissimilar incompatible materials due to complex metallurgical interactions at the materials' interface during melting and solidification phases. Such incomplete metallurgical reactions lead to brittle intermetallic phases, and thermally induced stresses result in bonding issues like cracking delamination or large porosity. This was evident during laser butt welding of titanium alloy to stainless steel [95], **Fig. 6a**, and fiber laser welding of Ti6Al4V and Inconel 718 alloys [99] without filler metal. Even by offsetting laser beam towards one side of the base materials to control metallurgical reactions in the melt-pool and improve weld quality, detrimental brittle intermetallic phases were formed, which led to the low bond strength of the joint. Also, similar bonding issues and failure characteristics were observed during AM processing of immiscible dissimilar materials through a direct deposition. For example, cracking and delamination features occurred during direct deposition of Inconel 718 on titanium alloy material [13,100,101] and Ti-alloy with stainless steel materials [44,102].

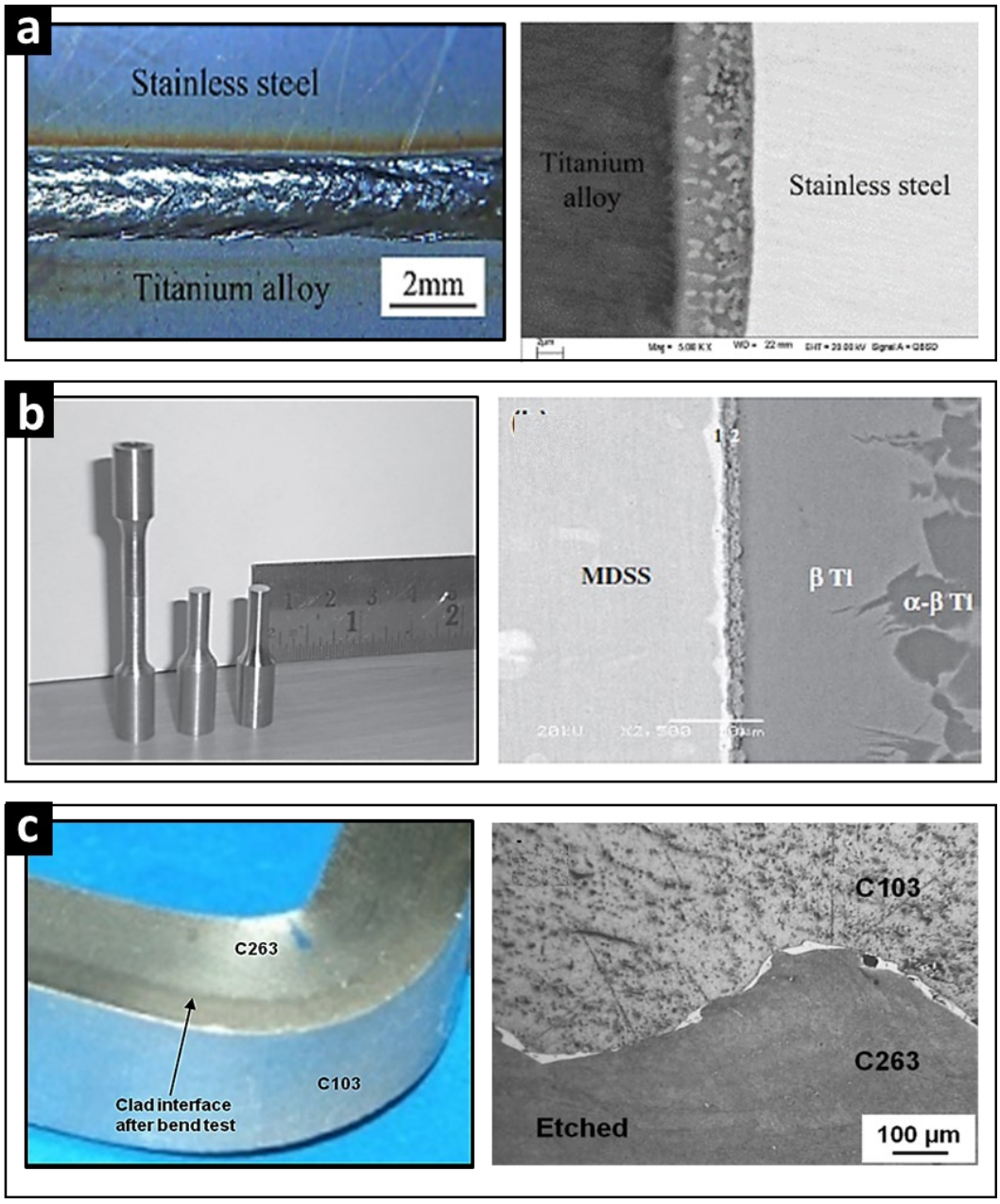

Figure 6. Directly bonded bimetallic materials via different joining processes: (a) Laser butt welding of titanium alloy to stainless steel [95], (b) Ti6Al4V and micro duplex stainless steel diffusion bonded joints [96], (c) Explosive cladding C103 niobium alloy over C263 nimonic alloy [97].

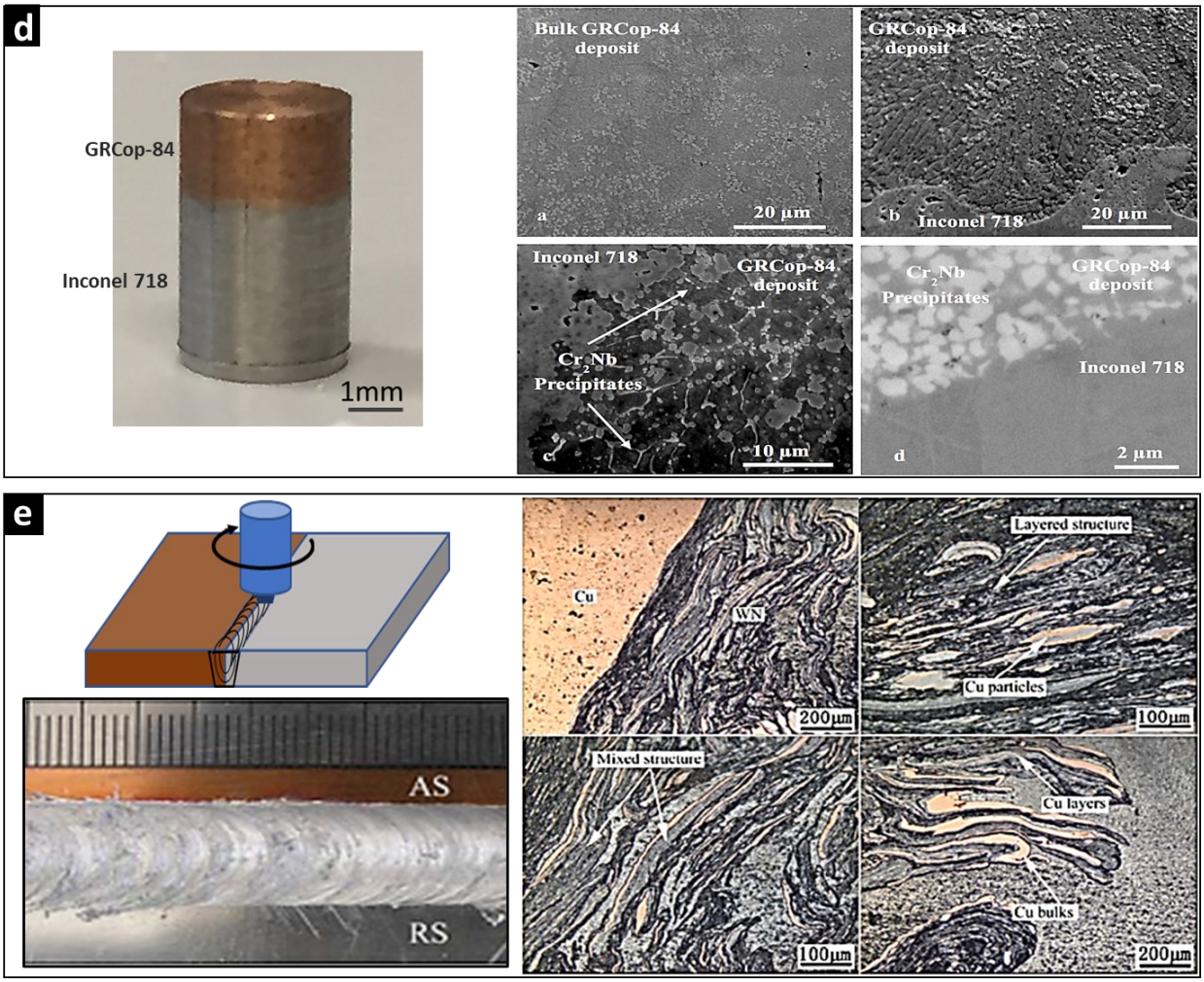

Figure 6 (cont.). (d) In 718/GRCop-84 bimetallic structure via LENS™ system [43], (e) Dissimilar Al−Cu joints by friction stir welding [98].

4.2 Compositional gradation

The preceding section described the direct bonding technique as a cost-effective and straightforward method to develop bimetallic joints of compatible dissimilar metals. However, such joints are sometimes characterized by a well-defined interface. In most cases, they are susceptible to cracking and delamination features at the interfacial region due to sharp variation in properties. This issue could be mitigated through the compositional gradation approach. The technique involves gradually transitioning one material's composition into the other across the composite interface [103]. Compositionally graded structures (CGS), often called functionally gradient materials (FGMs), benefit more than single and directly bonded structures. FGM

processing creates the opportunity to use materials composition as a design tool for properties enhancement [104]. **Fig. 7** shows different bimetallic structures developed via this approach. For instance, a rocket nozzle-shaped structure made of titanium alloy/Nb materials [104], shown in **Fig. 7a**, was fabricated through a gradient composition at the structure's throat section. **Figs. 7b and c** show functionally graded TA15 to Inconel 718 materials [101] and a bimetallic joint of Inconel 718/GRCop-84 materials [43]. Processing of compositionally graded Inconel-steel multilayer material using powder bed fusion process has also been demonstrated, **Fig. 7d** [105].

Although compositional gradation technique alongside modified processing parameters has shown promise to manufacture bimetallic structures of some difficult-to-bond dissimilar materials [101], such technique is most suitable for compatible dissimilar metals. Practically, if two materials cannot bond directly, bonding them compositionally is also challenging [13,106]. CGS can be designed with stepwise material composition via pre-mixing or by smooth gradation through dynamically mixing. Both methods have been used extensively to develop desired property-specific bimetallic products. AM processed FGMs with smooth transitioning show evenly distributed properties across the mixing zone. Both thermally induced and residual stresses are primarily reduced on FGM structures, especially for parts used in high-temperature gradient regions. While DED systems are more suitable for compositional gradation processes, the powder bed system still poses critical challenges due to difficulties in mixed powders separation [14,105].

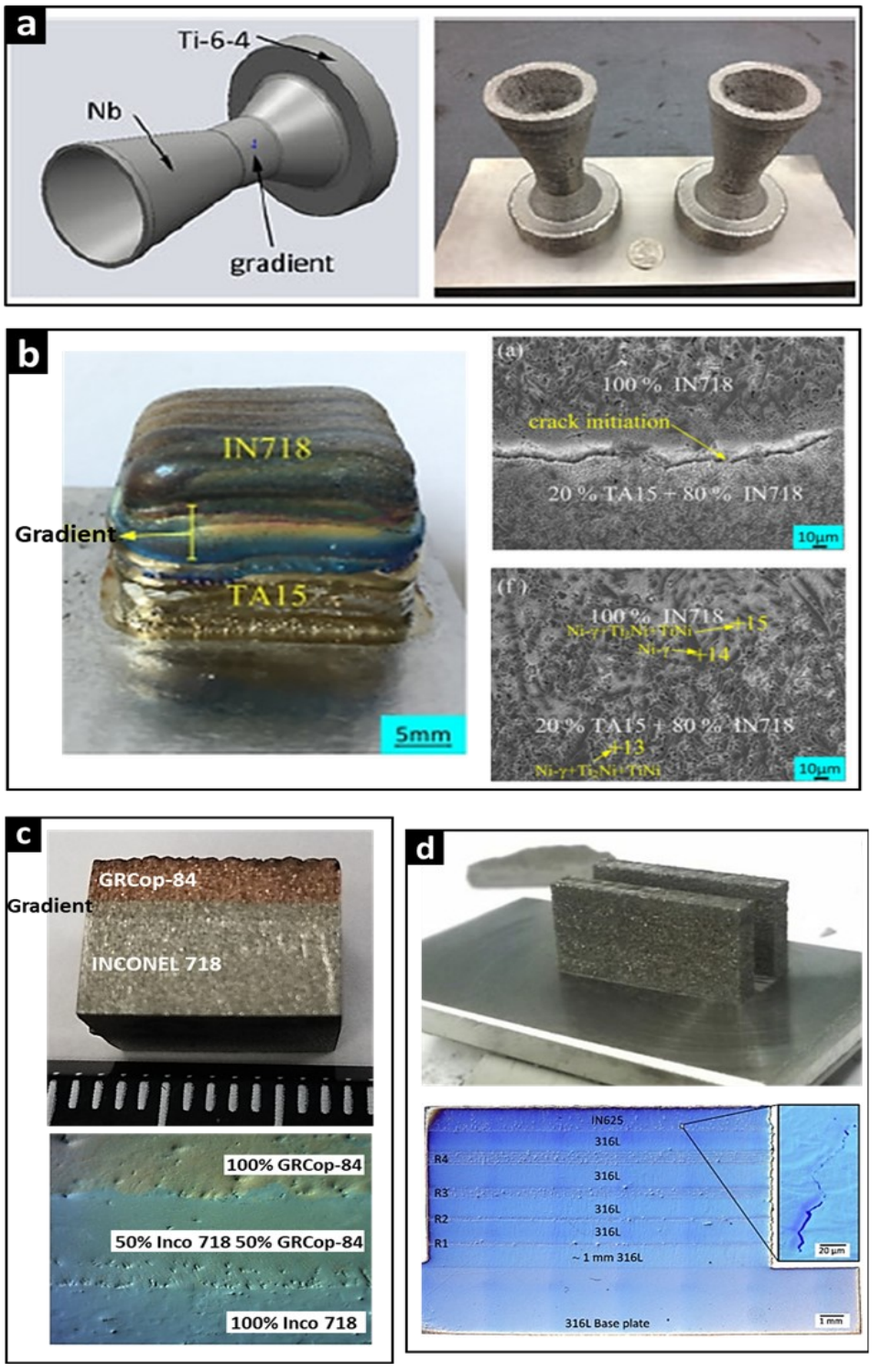

Figure 7. Compositionally graded bimetallic materials: (a) Compositionally graded Ti64 to Nb nozzle structure [104], (b) Crack elimination via base preheating and functional gradation of TA15 to Inconel718 materials [101], (c) In 718/GRCop-84 bimetallic structure via LENS™ system [43], (d) Inconel-steel multilayers by liquid dispersed metal powder bed fusion [105].

4.2.1 *Pre-mixing approach*: Pre-mixing involves a selective blending of a certain proportion of materials A and B in a mixer. A thorough blending of such powders is sometimes performed with ball milling media. This practice ensures that the powders are uniformly mixed. Powder mixing with milling media requires a high weight ratio of powders and should be carefully selected to avoid grinding, thus reducing the powder particle size distribution after ball milling. There are no general baseline criteria for a powder to ball weight ratio, as powder weight and desired compositions vary. In powder mixing without milling media, an extended period is required to obtain a homogenous mixture, and the duration depends on the powders' overall weight to be blended. Mixed powder composition can incrementally vary by weight %. For instance, pre-mixed powders containing 10 wt% of powder material A and 90 wt% of powder material B or 20 wt% of material A with 80 wt% of material B up to 50 wt % of both powders can be obtained. Each composition is poured into a powder feeder of an AM machine and deposited as a compositional layer with *in situ* alloying during build [107]. The sequence and number of depositions depend on desired design of the compositional gradation. The sequence can also be reversed, including powder materials' wt% combinations. **Figs. 7b and c** show functionally graded TA15 to Inconel 718 [101] structure and Inconel 718/GRCop-84 bimetallic joint [43] fabricated via pre-mixed powder strategy.

4.2.2 *Dynamically mixing approach*: Instead of pre-mixing powders in an external mixer before loading the blend into a single powder hopper, each powder is loaded into different hoppers, as most modern DED systems are equipped with multiple powder feeders. These powders are automatically mixed on the fly during the deposition, either at an integral mixing unit along the intersection of the powder delivery lines or the deposition head. This process is called dynamically mixing, where the bimetallic material's composition is varied through powder flow rate controlled by the powder feeder motors. For instance, hopper 1 is filled with powder material A, and hopper 2 is filled with powder B, then a 50/50 wt % of materials A and B can be deposited when the powder feeder motors are set to the same operational feed rate. Likewise, by increasing one of the motor's speeds and decreasing the other accordingly, the bimetallic material's composition can be varied as desired. Both Sahasrabudhe et al. [102] and Reichardt et al. [108] used this technique to fabricate bimetallic structures of titanium alloy (Ti64) and stainless-steel materials. Likewise, functionally graded alloy of SS304L and Inconel 625

materials [31] and bimetallic joint of Ti6Al4V+Al12Si materials were fabricated via a dynamically mixing process [49]. The input motor feed rate (rev/min) is typically calibrated to the powder flow rate in g/min experimentally to estimate the percentage composition by weight of each powder material in the mixture during deposition. However, such estimation is usually inaccurate after deposition because not all the powder materials blown into the melt pool region are melting. Some are blown off based on density variation. Such powders are mostly seen as waste/unused powders around the build chamber. Hence, post-process characterization is essential to fully quantify materials' percentage composition along the graded section of the part. This is one of the demerits of the dynamically mixing approach during FGMs processing.

4.3 Intermediate bond layer

While joining compatible dissimilar metals can be achieved easily via direct deposition and compositional gradation approaches, processing bimetallic joints of immiscible dissimilar materials using those techniques is difficult due to several factors. Of interest are (1) mismatch in metallurgical properties of the base materials, which promote the formation of a two-phase solid solution along with brittle intermetallic phases, leading to debonding features; and (2) wide variation in CTE of the base-metals which induces thermal/residual stresses during processing. These stresses aids crack initiation and propagation at the bimetallic joint's interface leading to delamination and, in most cases, complete failure of the joint [13,44,100–101]. Debonding phenomenon is usually evident during compositional gradation, as the base materials' immiscible elements inter-reacts at the gradient region of the bimetallic joint [13,104,109]. The formation of a two-phase solid solution could be attributed to the limited solubility of one element into another owing to thermodynamic mechanisms like higher entropy of mixing (ΔSmix) and enthalpy of mixing (ΔHmix) [110,111], as alloying elements reach equilibrium limit. Factors related to Hume-Rothery rules [112–114] also play a vital role. Hence, a study of the bimetallic base materials' main constituent elements' phase diagrams is essential.

For example, it is difficult to reliably join Ni-based alloy to Ti-based alloy or Ti-based alloy to stainless steel materials (Fe-based alloy) directly due to Ni and Fe with FCC crystal lattice structures and Ti with BCC structure are metallurgically incompatible. As such, they form brittle intermetallic phases of Ti_2Ni and $TiNi_3$ or FeTi and Fe_2Ti, as observed in the respective phase diagrams of Ni-Ti and Fe-Ti binary alloys systems [115]. To mitigate the challenges

associated with incompatible dissimilar metal bonding through direct joining or compositional gradation, an intermediate-bond-layer (IBL) build strategy was conceptualized [102]. The IBL is a third compatible material that acts as a bond-link and diffusion barrier to dissimilar metals' immiscible elements. This strategy has been the subject of intensive experimental research by many groups. Selection of candidate material to be used as an intermediate bond layer involved rigorous research exercise, as such material must possess unique characteristics to overcome the inherent issues associated with incompatible dissimilar metal bonding and improve bond strength. These characteristics are stated here as: (1) potential to impede the elemental diffusion between the two immiscible materials to mitigate the formation of brittle intermetallic phases; (2) ability to stabilize reaction product (brittle intermetallic phases) if formed during processing; (3) capacity to form stable phases, especially with the primary constituent elements of the dissimilar materials; and (4) ability to lower induced thermal stresses caused by thermophysical properties' mismatch at the bond region [13].

Single and multi-materials interlayers have been used to develop various bimetallic joints of difficult-to-bond materials. For example, single materials like nickel (Ni) [116,117], copper (Cu) [118–120], and silver (Ag) [121], including niobium (Nb) [44,122] have been used as interlayers to join titanium/Ti-alloy to various stainless-steel materials (**Fig. 8a**). Multi-materials used as interlayers include Ni-Cr [102] and Ag-Cu [123]. In fact, during the early stage of bimetallic joint development, Ni-Cr material was used as an interlayer to fabricate the bimetallic structure of SS410/Ti64 (**Fig. 8b**), opening up the possibilities of metal AM of multi-materials structures [102]. Meanwhile, multi-interlayered materials like Nb/Cu [124] have been used to join Inconel 718 to Ti-alloy (**Fig.8c**), while Ni/Cr [125] and Nb/Cu/Ni [126] for titanium to stainless steel bimetallic structures.

4.4 Compositional bond layer (CBL)

The concept of using an intermediate bond layer (IBL) is used for really difficult to join dissimilar metals. However, depending on the third material used as an interlayer, sharp interfaces may occur alongside other properties' variation at the bond region. To further improve the bonding capabilities of immiscible dissimilar metals, Onuike et al. (2018) [13] investigated a novel approach called compositional bond layer (CBL). This concept was first employed to

fabricate a bimetallic joint comprising a nickel-based alloy (Inconel 718) and titanium-based alloy (Ti6Al4V), **Fig. 8d**. CBL is a mixture of base metals with a third compatible material in a particular proportion. The approach differed from the multi-materials interlayers discussed in the previous section.

During the Inconel 718/Ti64 bimetallic structure processing, brittle intermetallic phases of Ti_2Ni and $TiNi_3$ were formed, leading to delamination, debonding, and failure of the joint. Hence, an interlayer was required, and vanadium carbide (VC) could form a single-phase solution with both Ni and Ti, the main constituent elements of Inconel 718 and Ti64, was selected. However, VC is an extremely hard material introducing a spike in hardness at the bond region if used as a single bond layer. Therefore, by depositing a mixture of VC + Inconel 718 and Ti64 materials in a specific ratio as a CBL, the high mechanical and thermophysical properties' variation like hardness spike and induced residual/thermal stresses at the bimetallic bond region was lowered. The CBL stabilized reaction products while enhancing the region's bonding capability to improve the bimetallic structure's mechanical reliability.

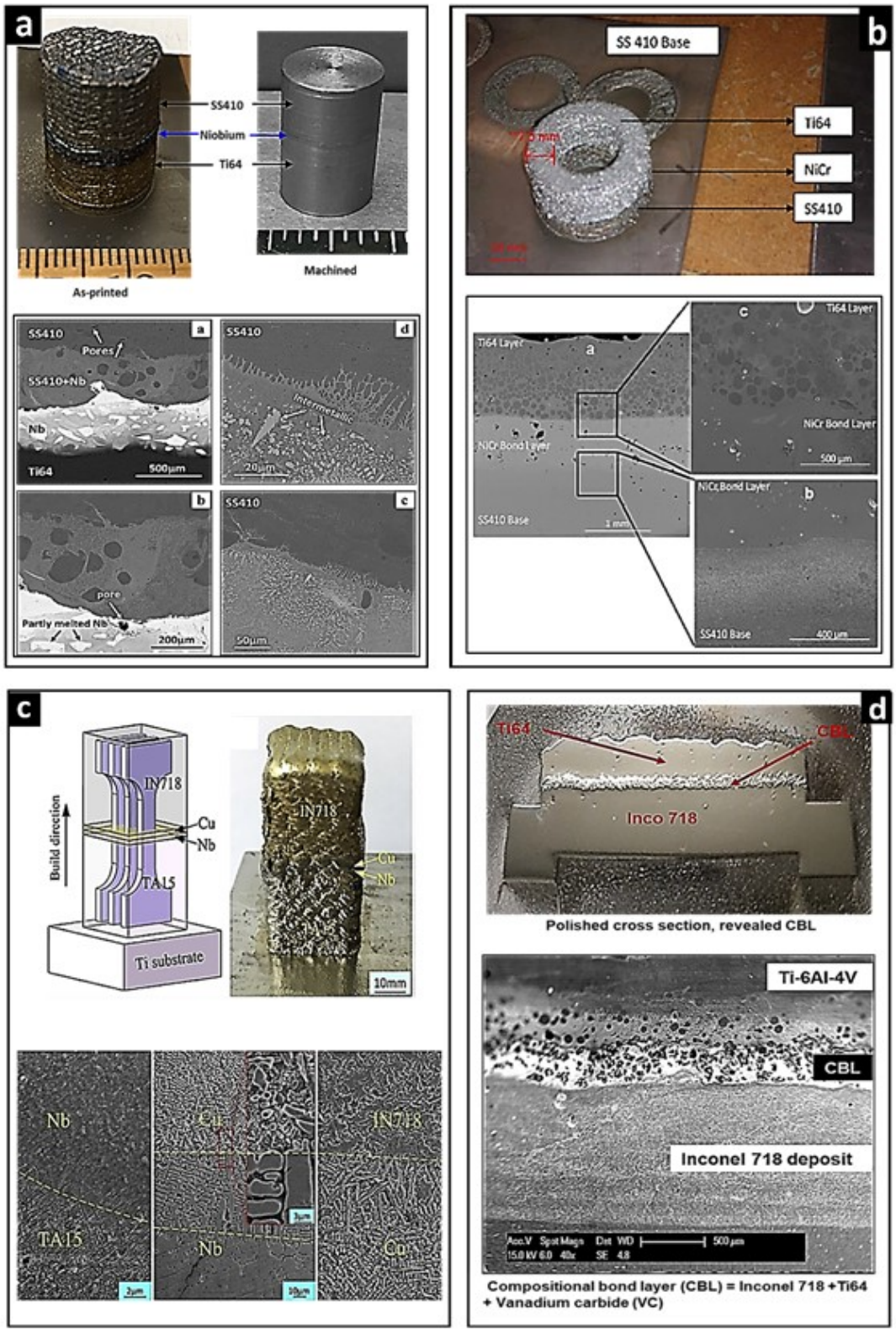

Figure 8. Bimetallic materials processed via Intermediate/Compositional bond layer approaches: (a) Functional bimetallic joints of Ti6Al4V to SS410 [44], (b) Stainless steel to

Ti bimetallic structure [102], (c) Laser AM of TA15 - Inconel 718 bimetallic structure via Nb/Cu multi-interlayer [124], (d) AM of Inconel 718 – Ti6Al4V bimetallic structures [13].

5.0 Critical challenges in processing bimetallic structure via additive manufacturing

At present, manufacturing bimetallic structures via AM is in its infancy, and there are many issues associated with processing such structures utilizing metal AM. These challenges can be clustered into material and process-related issues. Lack of standard software/programs capable of designing gradient material interfaces in bimetallic joint AM, including integration of such programs to HAM has been reported [91– 94] as well. The following sections extensively discuss other aspects of bimetallic joint characterization, such as microstructural analysis and bond strength-related issues.

5.1 Material compatibility issues

Preceding section discussions show that materials' characteristics, such as properties, chemical composition, and manufacturability, are essential for AM of bimetallic structures. During AM processing of immiscible dissimilar metals, the formation of brittle intermetallic phases, induced stresses, and defects at the interfacial region is inherent [14,85,90]. The use of IBL material to bond such metals proved promising, but such bimetallic joint interface involves complex mixing of materials with non-uniform distribution and properties across the region [13, 44,127,]. Selecting a compatible bond layer material to enhance the fabrication of a reliable bimetallic joint is tedious and sometimes not feasible [13,22,44,102,123,126]. The study of the alloy phase diagram provides a baseline for understanding alloy compositions and cues to material compatibility. A ternary phase diagram contains multiple equilibrium regions at different eutectic temperatures with complex elemental compositions. Such regions are difficult to analyze, including determining suitable alloy compositions that will mitigate the formation of brittle intermetallic phases. Therefore, sound knowledge of material science is essential to comprehend variances of the ternary phase system, including the sequence of equilibrium crystallization. Also, there is a need to expand the scope in establishing a comprehensive database for compatible materials specific as more advanced materials, including superalloys, are being developed.

5.2 Defects

Defects are undeniably the most common issue while using metal AM techniques to process bimetallic materials. Even though metal AM is a well-developed technology and can process multi-composition materials, the as-fabricated product may still have defects, especially at the interface. Defects are common in a single-material metal AM process, such as porosity, cracking, unmelted particles, etc. However, for bimetallic structures, apart from those defects, another set of defects generate due to compositional variations within the structure. **Fig. 9** demonstrates some common types of defects which occur at the interface of AM processed bimetallic materials. In general, the bimetallic material system can be categorized as homogenous and inhomogeneous based on the two metallic materials compatibility. For the homogeneous system (**Fig. 9a**), since the two metallic materials are compatible, which means a similar coefficient of thermal expansion (CTE), good solid solubility, and high diffusion ratio in each other, they can be joined by direct deposition. Some common defects such as unmelted particles and microvoids may occur at the homogenous bimetallic system interface due to the imprecise control while transitioning the material. Using metal AM technologies, especially the DED technology, to fabricate bimetallic structures typically requires switching processing parameters to manufacture different materials. Although current metal AM systems allow changing such processing parameters on the fly, it is still possible to have imprecise control issues, such as keeping unwanted powder feeding in the powder feed line and inaccurate laser power adjustment when changing laser power. These issues could cause a non-uniform melting of the fed materials at the interface and ultimately cause unmelted particles and micropore formation. Both **Fig. 9b** and **9c** are examples of the DED processed Ti/Ta bimetallic system. In **Fig. 9b**, the SEM and EDS images of the interface between a Ti6Al4V (Ti64) substrate and composition of DED processed 25% Ta/75% Ti64 section [128]. Unmelted Ta particles can be observed near the interface of these two sections. Additionally, **Fig. 9c** shows the Ta-coated Ti bimetallic structure's SEM image; micropores could be seen at the DED fabricated Ta section [129].

Using metal AM technologies to process an inhomogeneous bimetallic system is even more challenging than a homogeneous system. Since the two metallic materials to be processed are incompatible, they will likely form secondary phases at the interface. Most of the secondary phases are brittle intermetallic phases, plus metal AM is a rapid solidification process; these

conditions could easily result in weak bonding and cracks. Although many processing strategies for AM of dissimilar bimetallic structures are developed, it is impossible to eliminate the formation of the secondary phases. Moreover, the significant difference in CTE between the two metallic materials is another reason for the crack formation. **Fig. 9d** demonstrates a schematic of the common defects of an AM processed inhomogeneous bimetallic system. As mentioned, both cracks and secondary phases commonly occur at the interface of the two dissimilar materials. The cracks could be both external and internal. **Fig. 9e** shows the images of a DED processed Ti64/Al12Si bimetallic cylinder. This bimetallic structure was processed by applying the compositional gradation strategy and composed of five sections (Ti64 substrate, $(Ti64+Al12Si)_1$, pure Al12Si, $(Ti64+Al12Si)_2$ and pure Ti64). External cracks could be observed at the interface between the $(Ti64+Al12Si)_1$ and pure Al12Si section, as well as the $(Ti64+Al12Si)_2$ and pure Ti64 section. SEM images showed unmelted Ti64 particles at the transition sections. Complex secondary phases were also formed due to the laser-induced chemical reaction of the two materials. Phase analysis results showed $TiSi_2$ and Ti_3Al intermetallic phases were formed at the compositionally graded transition zones. The formation of these phases was caused by both compositional and energy input variations [49]. **Fig. 9f** demonstrates the as-fabricated DED processed Ti64/Inconel 718 bimetallic system. Due to significant CTE differences, the direct deposition technique found critical delamination between the two materials. Researchers switched to using a compositional bond layer with vanadium carbide (VC) to enhance the bond strength between Ti64 and Inconel 718. Although no significant cracks were found at the interface between the compositional bond layer and the pure Ti64 section, the SEM image showed that unmelted particles and micropores could still be seen, indicative of non-uniform melting at this region [13]. **Fig. 9g** shows the images of a DED fabricated SS 316L/Al12Si bimetallic system which contains four different sections (pure SS 316l, $(SS\ 316L+Al12Si)_1$, $(SS\ 316L+Al12Si)_2$, and pure Al12Si) by applying compositional gradation strategy. Horizontal cracks could be observed at the interface between the pure SS 316L and $(SS\ 316L+Al12Si)_1$ section. The cross-section image of the as-fabricated SS 316L/Al12Si bimetallic structure shows that the crack penetrated the entire interface. The crack formation was caused by a large amount of brittle intermetallic phases. Researchers improved the design by reducing the number of transition layers to reduce secondary phase formation. However, internal micro-cracks could still

be observed at the interface based on the microscopic image. The XRD analysis confirmed that multiple intermetallic phases such as FeAl, Fe_2Al_5, and $FeAl_3$ were formed at the interface [45].

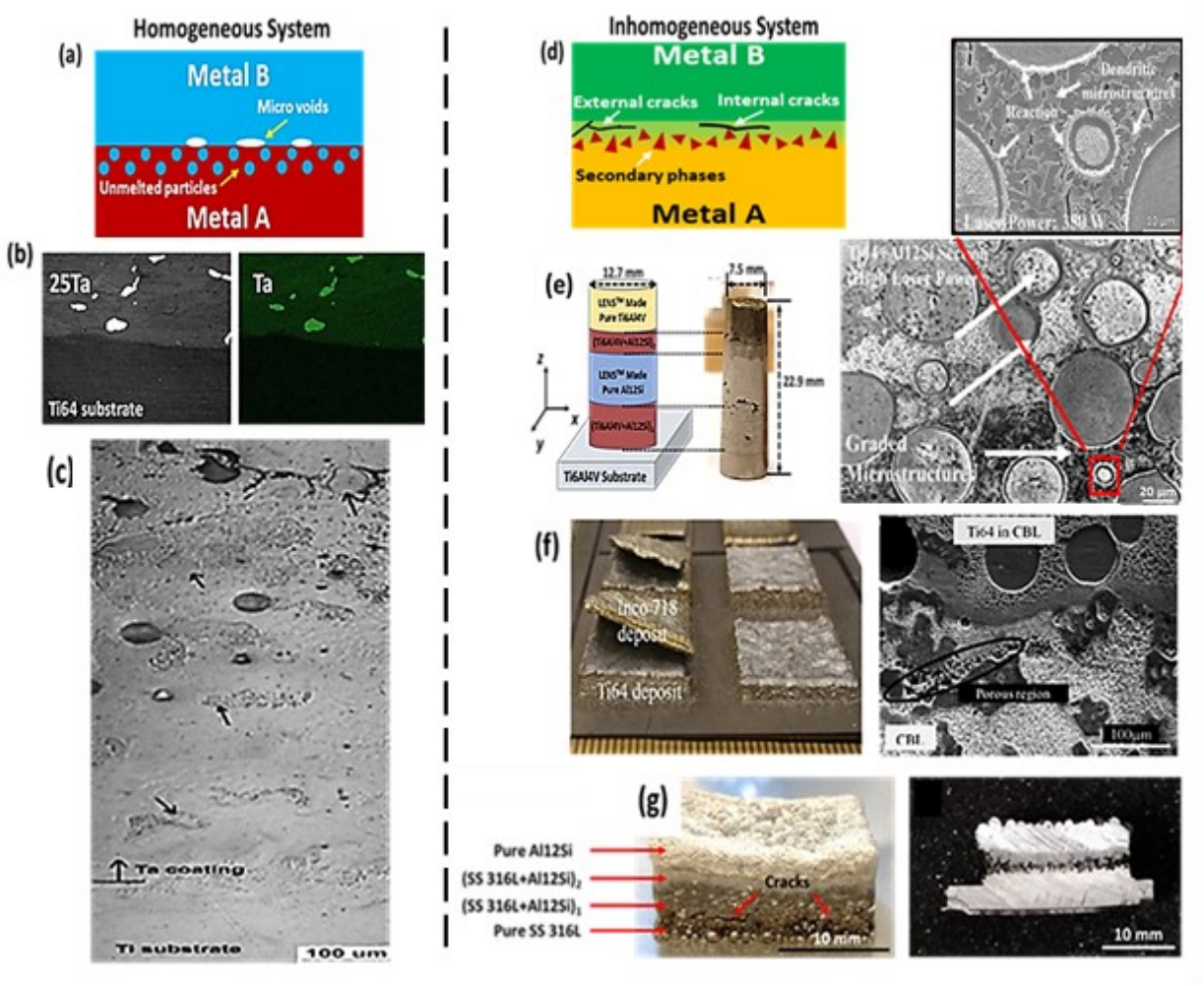

Figure 9. (a) Schematic of common defects that occur at the metal AM interface processed homogeneous bimetallic system. (b) SEM and EDS images of the interface between Ti6Al4V substrate/25%Ta-75%Ti system processed by DED method [127]. (c) SEM image of a DED processed Ti/Ta bimetallic system [129]. (d) Schematic of common defects that occur at the interface of metal AM processed inhomogeneous bimetallic system. (e) Images of a DED processed Ti64/Al12Si bimetallic system and the microstructures at the interface [49]. (f) Images of the as-fabricated Ti64/Inconel 718 bimetallic system processed by DED method and the microstructures at the interface between the compositional bonding layer and pure Ti64 section [13]. (g) Images of a DED processed SS 316L/Al12Si bimetallic system, cross-section image of

the as-fabricated SS 316L/Al12Si bimetallic, and the microphotograph of the interface between the SS 316L and Al12Si [45].

5.3 Processing parameters optimization

Processing parameters are the critical factors for metal AM to control part quality and performance. Generally, the processing parameters need to be tested and optimized when using metal AM to process metallic materials, especially novel materials. Most laser-based metals AM systems allow users to control the processing parameters such as laser power, the feed rate of feedstock materials, and laser scan speed. Some advanced systems even allow adjusting the processing parameters on the fly based on print quality. Multiple strategies could be created to fabricate bimetallic structures using metal AM technologies by taking these advantages. However, there are some challenges with selecting processing parameters for bimetallic structures.

The first challenge is the lack of standards. Unlike many traditional manufacturing methods with a mature processing standard, the processing parameters for metal AM are machine and method-dependent. It means the processing parameters for the same metallic material using different laser-based metal AM technologies or the same technology, but a different machine could be different. **Table 2** summarizes some reported processing parameters of selective laser melting (SLM) and DED processed Ti6Al4V. Comparing these two methods is that both SLM and DED are laser-based metal AM technology, and they all use metal powder as feedstock material. According to the table, the processing parameters for Ti6Al4V fabrication using SLM and DED methods are different. In general, the laser power used for processing Ti6Al4V by SLM is lower than DED, and the scan speed is much faster than DED. Understandably, SLM is more adapted in current manufacturing industries, and the time cost needs to be considered a priority. However, even using the same metal AM methods, the processing parameters for processing Ti6Al4V still significantly differ. Specifically, for using SLM to process Ti6Al4V, the selected laser power could vary from 157 W to 340 W, and the scan speed can be from 225 mm/s to 1250 mm/s; for using DED to process Ti6Al4V, the chosen laser power have a range from 330 W to 2100 W, and the powder feed rate can be from 2 g/min up to 14 g/min [130–139]. Despite the variation of the feedstock material's quality, the

processing parameters for a specific metallic material using metal AM technology are not only method depended but also machine depended.

Table 2. A summary of processing parameters for SLM and DED fabricated Ti6Al4V and bimetallic structures using Ti6Al4V.

Material	Processing methods	Reporters	Processing Parameters			
			Laser power	Scan speed	Powder feed rate	Layer thickness
Ti6Al4V	SLM	Ju et al. [130]	280 W	1200 mm/s	-	30 µm
		Denti et al. [131]	340 W	1250 mm/s	-	30 µm
		Kasperovich et al. [132]	200 W	1250 mm/s	-	40 µm
		Simonelli et al. [134]	157 W	225 mm/s	-	50 µm
		Mertens et al. [135]	175 W	710 mm/s	-	30 µm
	DED	Bandyopadhyay et al. [133]	445 W	13-20 mm/s	14 g/min	0.152-0.178 mm
		Liu et al. [136]	330 W	15 mm/s	2 g/min	-
		Buciumeanu et al. [137]	350 W	12.7-16.9 mm/s	9.36 g/min	0.02 mm
		Xue et al. [137]	2100 W	12 mm/s	14 g/min	-
		Bonaiti et al. [139]	710/800/940 W	10 mm/s	7.2 g/min	-
Ti6Al4V + Al12Si		Zhang et al. [49]	300 – 425 W	10 – 16.25 mm/s	6 – 17.3 g/min	180 µm
Ti6Al4V + Inconel 718		Onuike et al. [13]	375 - 450 W	5 - 8.3 mm/s	-	200 – 250 µm
Ti6Al4V + SS410		Onuike et al. [44]	375 - 450 W	5 - 6.7 mm/s	-	150 - 200 µm

The second challenge is the optimization of processing parameters. As previously mentioned, the processing parameters are highly dependent on each machine. Therefore, optimizing the processing parameters for metal AM requires a series of experiments. It is even more challenging to optimize the processing parameters of AM of bimetallic structures, especially for joining two dissimilar materials. Since the dissimilar materials cannot be directly joined together due to the significant difference in the thermal properties, a compositionally

graded transition or a bonding material is needed. The processing parameters must be adjusted while fabricating the transition region to get an interface with minimized defects. Chen et al. [72] investigated process parameters' influence on the interfacial characterization of selective laser melting SS 316L/CuSn10 bimetallic. **Fig. 10a** and **10b** show the as-fabricated SS 316L/CuSn10 samples and the design of the bimetallic structure. The SLM processed bimetallic structure composed a pure SS 316L section, interfacial layers (20 layers), and pure CuSn10 section. The researchers performed the three factors and five orthogonal experiments on the interfacial layers to study the effects of laser power, laser scan speed, and hatch space on fabrication and performance optimization. Volumetric energy input density (E_v) was used to describe the effects of processing parameters which shows as follow:

$$E_v = \frac{P}{vTh} \quad (1)$$

Where E_v (J/mm^3) is the laser energy input density, P (W) is laser power, v (mm/s) is scanning speed, T (mm) is hatch space, and h (mm) is layer thickness. **Fig. 10c** and **10d** show the results of orthogonal experiments, in which the conditions were P = 260 W and v = 600 mm/s correspondingly. For condition 1 (**Fig. 10c** P = 260 W), by adjusting both laser scan speed and hatch distance, the energy input density varied from 101.36 J/mm^3 to 231.11 J/mm^3. The results showed severe cracking at the interface when the energy input density was low due to incomplete melting. The defects were significantly minimized by increasing the energy input density (231.11 J/mm^3), but pores and microcracks could still be found in the interfacial region. Similar findings were also observed in condition 2 (**Fig. 10** v = 600 mm/s). Under condition 2, the laser scan speed remained constant at 600 mm/s. By controlling the laser power and hatch space, the energy input density ranged from 180.56 J/mm^3 to 251.85 J/mm^3. Only pores were observed at the interface when low energy input density was applied. Improvement was made by increasing the energy input density to minimize the defects, but vertical microcracks could still be seen at the interfacial area when the highest energy input density (251.85 J/mm^3) was applied [72]. Other papers also discussed the metal AM defects' and their relationship to processing parameters [120,140–143]. At present, obtaining a defect-free/minimal defects AM processed bimetallic structure is still challenging and requires extensive experimentation for processing parameter optimization.

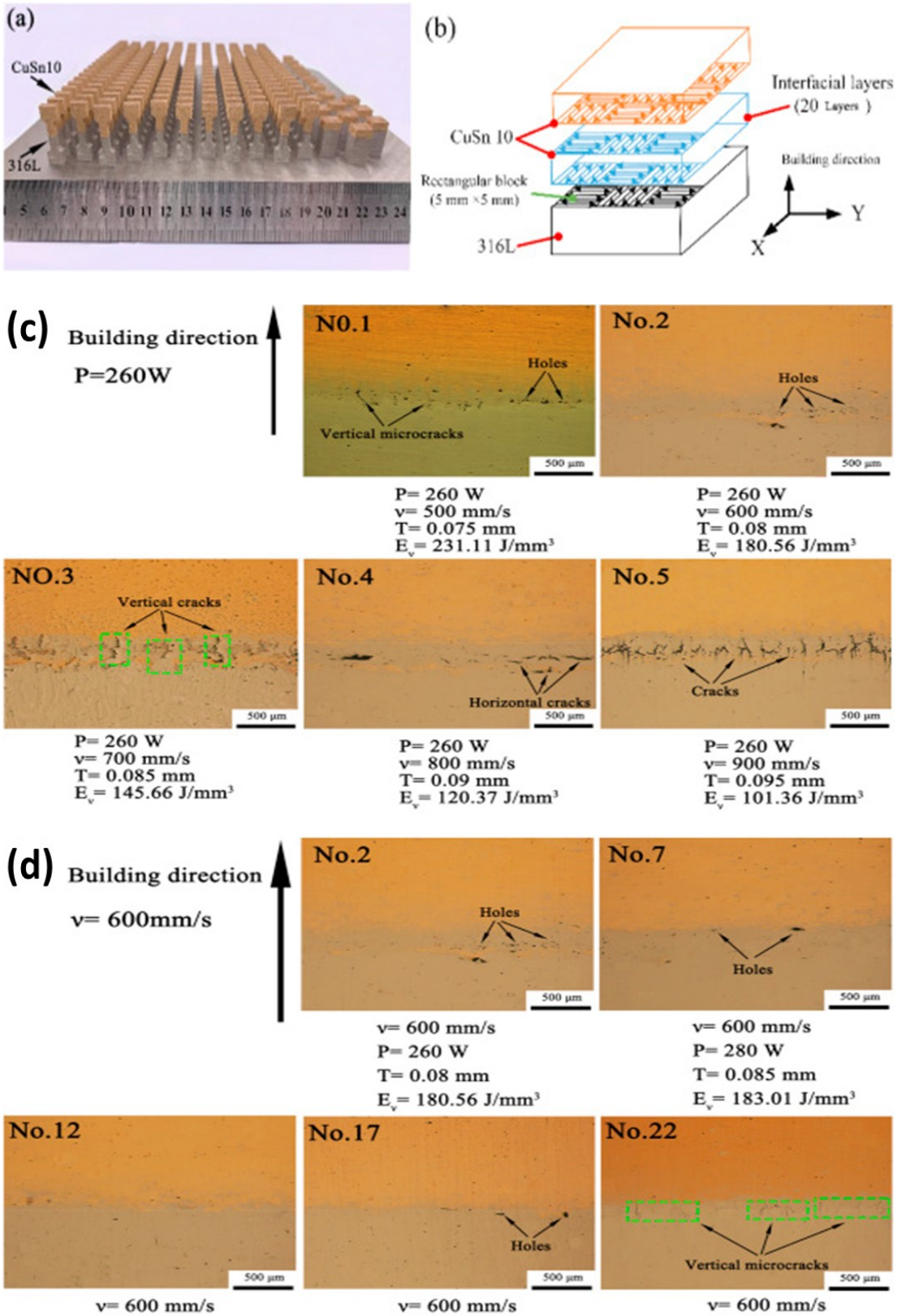
(a)
CuSn10
316L
(b)
Interfacial layers
(20 Layers)
CuSn 10
Rectangular block
(5 mm ×5 mm)
316L
Building direction
Y
X
(c)
Building direction
P=260W
N0.1
Holes
Vertical microcracks
500 μm
P= 260 W
v= 500 mm/s
T= 0.075 mm
E_v= 231.11 J/mm³
No.2
Holes
500 μm
P= 260 W
v= 600 mm/s
T= 0.08 mm
E_v= 180.56 J/mm³
NO.3
Vertical cracks
500 μm
P= 260 W
v= 700 mm/s
T= 0.085 mm
E_v= 145.66 J/mm³
No.4
Horizontal cracks
500 μm
P= 260 W
v= 800 mm/s
T= 0.09 mm
E_v= 120.37 J/mm³
No.5
Cracks
500 μm
P= 260 W
v= 900 mm/s
T= 0.095 mm
E_v= 101.36 J/mm³
(d)
Building direction
v= 600mm/s
No.2
Holes
500 μm
v= 600 mm/s
P= 260 W
T= 0.08 mm
E_v= 180.56 J/mm³
No.7
Holes
500 μm
v= 600 mm/s
P= 280 W
T= 0.085 mm
E_v= 183.01 J/mm³
No.12
500 μm
v= 600 mm/s
P= 300 W
T= 0.09 mm
E_v= 185.19 J/mm³
No.17
Holes
500 μm
v= 600 mm/s
P= 320 W
T= 0.095 mm
E_v= 187.13 J/mm³
No.22
Vertical microcracks
500 μm
v= 600 mm/s
P= 340 W
T= 0.075 mm
E_v= 251.85 J/mm³

Figure 10. (a) As-fabricated SS316L/CuSn10 bimetallic structures processed via SLM. (b) The design of SLM processed SS 316L/CuSn10 bimetallic structure. Optical microimages of the interface in the SLM fabricated steel/bronze bimetallic structures: (c) when the laser power is 260 W, (d) when the scanning speed is 600 mm/s [72].

6.0 Microstructure evolution of AM processed bimetallic structures

Understanding the microstructure evolution in AM processed bimetallic structures can aid the processing parameters optimization and predict or even tailor the fabricated product's properties. The microstructure of AM processed bimetallic structures could be significantly affected by the processing parameters and compositional variation. The microstructure variation can ultimately impact the mechanical properties of the materials. The most commonly processed AM bimetallic joint systems and extensively researched are Fe- and Ti-based alloy materials; others include Ni- and Cu-based alloys.

6.1 Fe-based bimetallic systems

Since AM processed bimetallic materials have gained much attention recently, many bimetallic systems' microstructure evolution was studied and reported. Demir et al. studied an SLM-made Fe/Al12Si bimetallic system [144]. The Fe/Al12Si bimetallic was fabricated by a dual powder feeders SLM system and consisted of three sections: pure Fe, 55 vol% Fe/45 vol% Al12Si, and pure Al12Si sections (**Fig. 11a**). The hatch distance for all sections was set as 110 μm. The laser power and scan speed used for fabricated each section were: pure Fe (236 W, 120 mm/s), 55 vol% Fe/45 vol% Al12Si (142/236 W, 33/50/67 mm/s), pure Al12Si (236 W, 40 mm/s). The density analysis showed that the as-fabricated Fe/Al12Si bimetallic had a high density ($\rho > 99\%$). The microstructures in each section were characterized and depicted as (**Fig. 11a**). Due to rapid cooling cycles, fine microstructures were found in pure Fe and Al12Si sections. However, large grains with a grain size range of 50 to 70 μm were obtained in the Fe/Al12Si bimetallic composition zone. In a previous study, using a smaller laser beam diameter, low laser power, and high scan speed could result in finer grains of an SLM fabricated Fe/Al material with pre-alloyed Fe/Al powder [145]. The microstructural images suggested that FeAl intermetallic phases were formed *in situ* during the SLM processing. Another study conducted by

Liu et al. demonstrated the interfacial microstructures of an SLM processed SS 316L/C18400 copper alloy bimetallic [146]. The pure SS 316L section was first processed with a laser power of 125 W and a scan speed of 150 mm/s; the pure copper C18400 alloy was directly deposited on top of the SS 316L section with a laser power of 300 W and a scan speed of 400 mm/s. An intermixed zone assisted with diffusion could be found at the SS and copper alloy interface. The measurement showed that the intermixed zone had a thickness of ~750 μm, which indicated significant dilution between these two materials. The pure SS 316L section showed a uniform and crack-free morphology. However, vertical cracks were observed at the interface between SS and copper. The pure copper section showed a large porosity because of insufficient melting due to copper alloy's high laser reflectivity and thermal conductivity. The SEM analysis was performed at the SLM processed SS 316L/Cu alloy interface to study microstructure evolution (**Fig. 11b**). Three different zones: zone A: pure SS, zone B: SS 316L/Cu interface, and zone C: pure Cu alloy, were selected and analyzed. The pure SS section had both ultrafine grains and coarse elongated grains. The microstructure at the SS 316L/Cu interface showed a mixture of fine SS and feathery copper. In zone C, the feathery microstructures were dominated. The EBSD result showed that the grains' random orientation occurred at the SS 316L/Cu alloy interface. Since the SLM technique is a layer-by-layer fabrication method, grain growth in previously fabricated layers could occur due to multiple thermal excursions. Furthermore, the melt pool underwent supercooling as rapid solidification was involved in the SLM processing. Although Fe-Cu were completely miscible in the liquid state, the high cooling rate separated the liquid Fe and liquid Cu, resulting in an incomplete diffusion. After the solidification, the Cu alloy solidified as the matrix, and the SS formed as fine spherical precipitates (**Fig. 11b**).

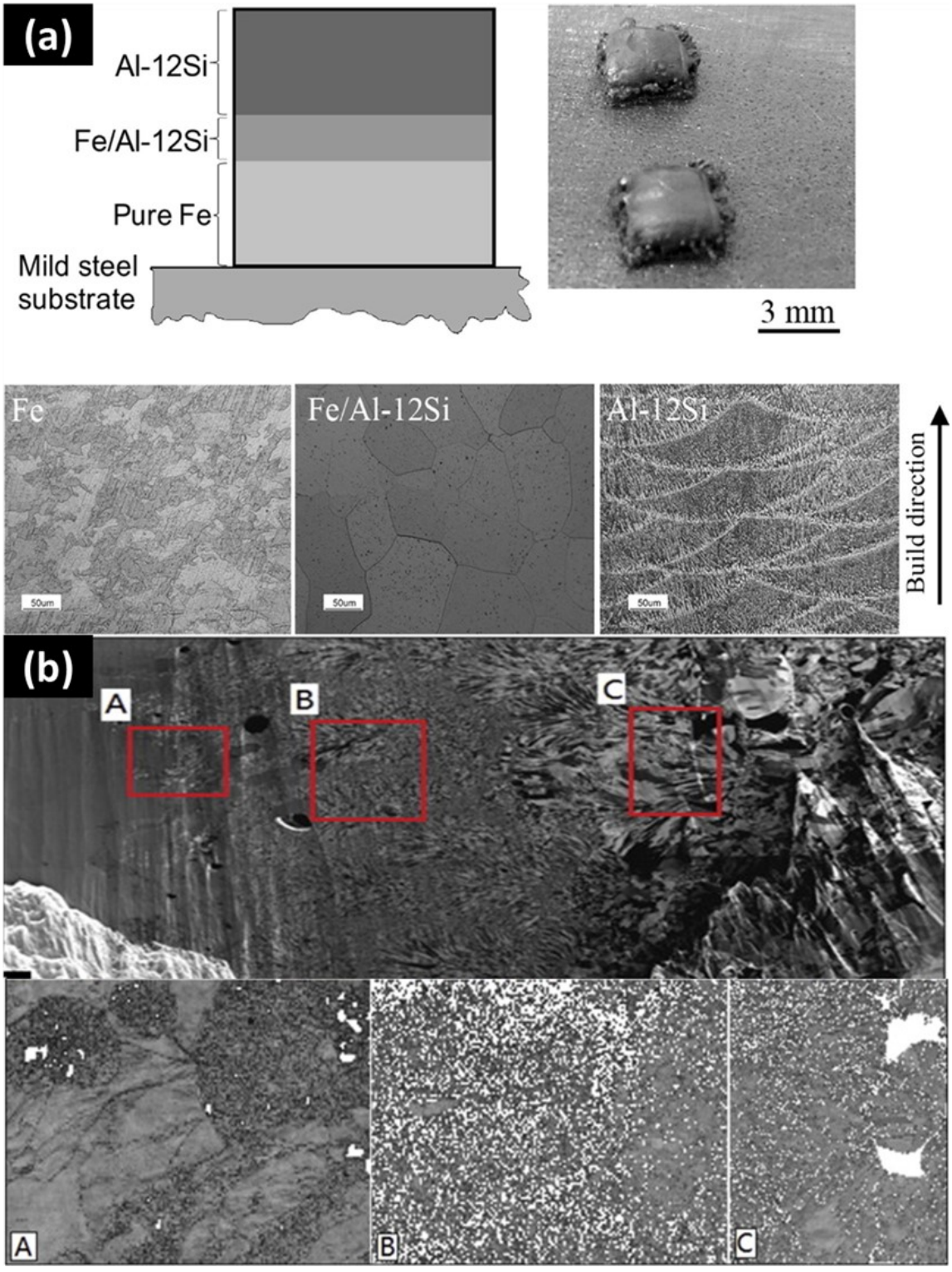

Figure 11. (a) Design, as-fabricated and cross-sectional microstructures of the SLM processed Fe/Al12Si bimetallic component [144]. (b) SEM results of the SLM processed SS 316L/C18400 copper alloy bimetallic material [146].

Ahsan et al. [147] studied the microstructure evolution of a wire-arc additive manufactured (WAAM) SS316L/Inconel 625 bimetallic structure (**Fig.12a**). The ampere and voltage used for fabricating the SS316L side were 200 A and 13.1V. The ampere and voltage utilized for processing the Inconel 625 side were 148 A and 14.5V, respectively. Other parameters, such as moving speed, torching angle, travel angle, and layer thickness, were fixed as 600 mm/min, 90°, 90°, and 3 mm. The bimetallic structure was deposited on a low-carbon steel substrate. **Fig. 12b** demonstrates the SEM images, EDS mappings, and EBSD results of the microstructures on the SS316L side. According to the results, the columnar grains with an orientation towards the build direction were obtained in this section. The higher magnification image reveals vermicular δ-ferrites (dark region) in an austenite matrix (light region). The formation of this type of microstructures suggested a ferrite-austenite (FA) type of solidification with a moderate cooling rate. In FA solidification mode, austinites started to form along with the ferrite cell and dendrite boundaries through a peritectic-eutectic reaction at the end of primary ferrite solidification. As the molten pool cooled through the ferrite + austenite field, the ferrites became unstable, and the austenite phase consumed the ferrites until the ferrites were sufficiently rich in ferrite-promoting elements (Cr and Mo) and depleted in austenite-promoting elements (Ni) [147,148]. Based on the elemental mappings, the δ-ferrites showed a higher concentration of Cr and Mo. Ni was the dominant element in the austenite matrix which supports the aforementioned microstructure-transformation mechanism. The EBSD results identified a few large grains in the SS316L section, although the grain-size distribution showed a higher number fraction of smaller grains. Based on the results of the EBSD and the pole figures, <001> grain growth direction was suggested in the SS316L section. **Fig. 12c** shows the images of the microstructures, EDS mappings and the EBSD results at the interface of the SS316L/Inconel 625 bimetallic structure. Unique microstructures were showed on each side. The EDS results showed that Cr was distributed across the interface homogeneously. Additionally, Ni, Nb, and Mo had a higher concentration on the Inconel side, whereas the SS316L was rich in Fe. Moreover, a slight diffusion of Fe was obtained on the Inconel side. No elemental segregation at the interface was seen. The EBSD analysis results showed a continuous grain growth in the <001> direction. No crystallographic discontinuity growth was observed since both SS316L and Inconel 625 had an austenitic FFC structure with a preferred growth orientation of <001>. **Fig. 12d** demonstrates the images of microstructures, EDS mapping and the EBSD results on the Inconel 625 side. The

SEM images showed the microstructures were fully austenitic with three distinct boundaries, which were solidification grain boundary (SGB), solidification subgrain boundaries (SSGBs), and migrated grain boundaries (MGBs). These grain boundaries could be clearly distinguished due to compositional differences compared to the bulk microstructure. Laves and γ-austenite phases were found in the Inconel 625 section. The EDS mappings showed higher Nb and Mo concentration in Laves phase. The EBSD results showed periodic alternations between more refined and coarse columnar grains due to the difference in temperature and cooling rate within a single layer [149]. The pole figures suggested a strong directional grain growth direction of <001> along with the build direction.

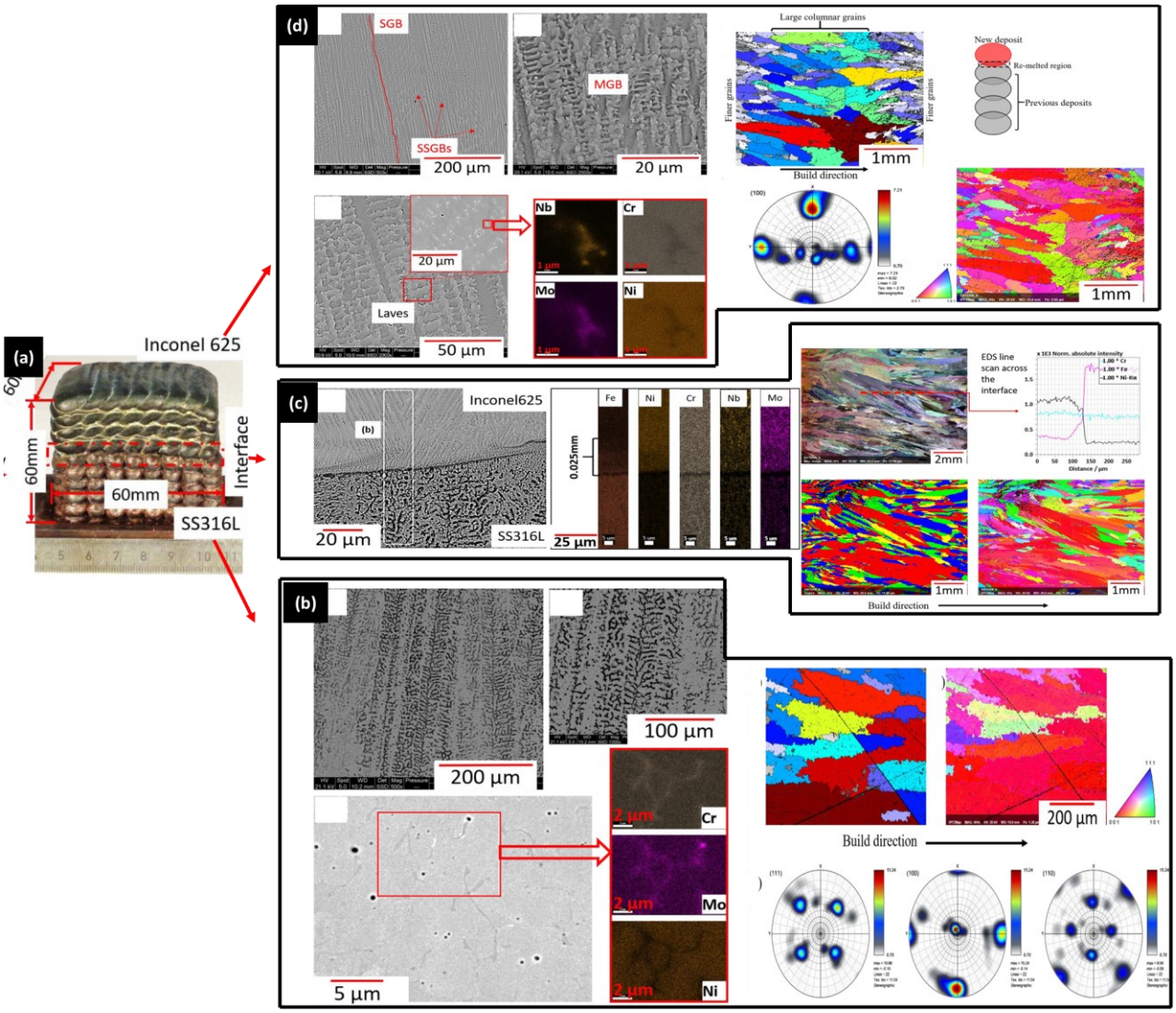

Figure 12. (a) Wire-arc additive manufactured (WAAM) SS316L/Inconel 625 bimetallic structure. (b) SEM images, EDS mappings, and EBSD results of the microstructures on the SS316L side. (c) SEM image, EDS mappings, and EBSD results of the microstructures at the interface. (d) SEM images, EDS mappings, and EBSD results of the microstructures on the Inconel 625 side [147].

6.2 Ti-based bimetallic systems

The microstructures of the DED fabricated Ti6Al4V/V and Ti6Al4V/Mo compositionally graded materials were studied by Collins et al. [141]. The energy density was utilized from 30000 – 100000 W/cm^2 to fabricate the Ti6Al4V/V and Ti6Al4V/Mo FGMs on the Ti6Al4V substrate. A set of backscattered SEM images at the cross-section of Ti6Al4V/V FGM with increasing V content is shown in **Fig. 13i**. Widmanstätten α-Ti laths with a small volume fraction of β-Ti were seen at the composition of Ti-1.8% V. α-Ti laths and β-Ti grains were also found in Ti-3% V section. Additionally, the β-Ti grain boundary was decorated with α-Ti in this section. A significant microstructure change was found when the V increased to 5%. The addition of V decreased the volume fraction of the β-Ti and the average width of the α-Ti laths. The resulted microstructure consisted of intricately mixed α-Ti laths, called basketweave microstructures. In the Ti-6.8% V section, the increased V content resulted in a bimodal mixture of coarse α-Ti precipitates and further refined the distribution of α-Ti laths. This phenomenon was possibly caused by the solid-state annealing on existing layers during the laser processing, resulting in secondary precipitation within the retained β matrix. Therefore, the coarse α-precipitates was caused by primary precipitation of α within β during the initial deposition, and the fine α-Ti was a result of secondary precipitation during post-deposition annealing. The microstructures in the Ti-8% V section were similar to the Ti-6.8% V section but with a smaller primary α-Ti laths. When the V content increased to 10%, uniformly distributed α-Ti laths of the same size were found. A significant decrease of α-Ti in volume fraction was obtained when the V content was enriched to 10%. Further decrease in volume fraction of α-Ti laths was also seen in the Ti-12% V section. Also, the size of α-Ti laths was further refined, and the β-Ti grain boundaries were decorated by discrete α-Ti. The microstructure in Ti-17% V showed fully stabilized β-Ti. The microstructure evolution of the DED processed Ti/Mo FGM is shown in **Fig. 13ii**. The trend in microstructure variation was similar to the DED made Ti/V FGM. Widmanstätten α-Ti laths

were the predominant microstructure when the Mo concentration was low. When the Mo content increased to 5.5%, the volume fraction of β-Ti was significantly increased, and the refined α-Ti precipitates were uniformly distributed within the β matrix. For the compositions with high Mo concentration (>5% Mo), the thickness of the α-Ti was reduced substantially. The precipitation along the grain boundaries became more discretized and eventually became equiaxed. Similar results were also obtained by Schneider-Maunoury et al. [150]. **Fig. 13iii** illustrates the EBSD results of a DED-CLAD processed Ti/Mo FGM with a variation of 0% - 20% Mo concentrate from bottom to top [150]. The pure Ti section presented large columnar β-Ti grown towards the build direction with a texture of $<100>_{\beta}$. With Mo content's increase, a significant change of microstructures with the formation of equiaxed grains was observed. Moreover, the size of the equiaxed grains decreased with the further addition of Mo. The formation of finer equiaxed grain was caused by remelting the previous layer during the laser DED processing.

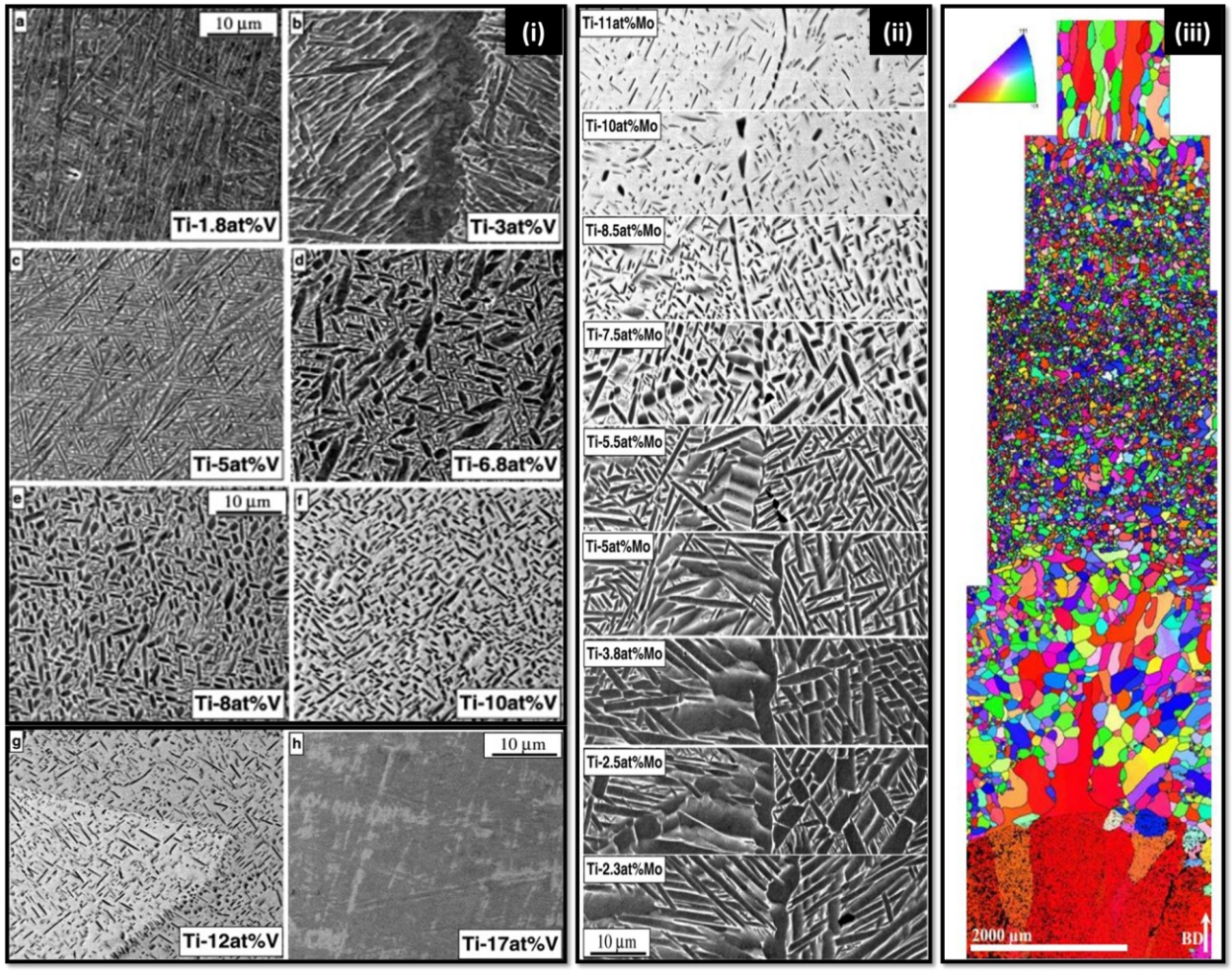

Figure 13. (i) Backscatter SEM images of the DED fabricated Ti/V FGM [141]. (ii) Backscatter SEM images of the DED fabricated Ti/Mo FGM [141]. (iii) EBSD results of a DED-CLAD processed Ti/Mo FGM with a variation of 0% - 20% Mo concentrate from bottom to top [150].

Xu et al. [151] utilized an Nb bond layer to fabricate a Ti6Al4V/$Al_{6.21}Cu$ bimetallic structure via WAAM with a cold metal transfer technique. The wire feed speeds of Ti6Al4V and $Al_{6.21}Cu$ were set as 8 m/min and 4 m/min, respectively. Initially, 9 layers of Ti6Al4V were deposited on the Ti substrate. Then the top of the deposited Ti6Al4V was grounded to obtain a flat surface for fixing the Nb foil. The Nb interlayer was joined with the deposited Ti6Al4V by tungsten inert gas (TIG) welding. Finally, 19 layers of $Al_{6.21}Cu$ were deposited on top of the polished Nb interlayer. **Fig. 14a** illustrates the EDS mappings at the interface of the WAAM made Ti/Al bimetallic structure. The results show that a certain amount of Nb was dissolved in the Ti6Al4V layer and evenly distributed. No other elements were obtained in the Nb interlayer besides Nb, suggesting that the Nb interlayer served as a diffusion barrier to prevent the diffusion of Ti and Al and thereby inhibited the formation of Ti-Al brittle intermetallic compounds. In addition, a small amount of Nb was found in the $Al_{6.21}Cu$ section due to the high melting point of Nb and low energy input during the $Al_{6.21}Cu$ deposition on Nb. The Cu element was enriched at grain boundaries in the $Al_{6.21}Cu$ section. **Fig. 14b** demonstrates the SEM images at the interface of the WAAM made Ti/Al bimetallic with and without Nb interlayer. The cross-section image displays the formation of pores in Al alloy closed to the interface due to the assimilation of hydrogen (**Fig. 14b-i**). In **Fig. 14b-ii**, cellular grains were found in the $Al_{6.21}Cu$ section. **Fig. 14b-iii** shows the white network-like phase of Al-Cu eutectic (α-Al and Al_2Cu) was formed along the grain boundaries. Furthermore, an Al_3Nb reaction layer was formed with a thickness of 2-3 μm at the $Al_{6.21}Cu$/Nb interface. No visible defects could be seen at the interface. In **Fig. 14b-iv**, the acicular structures were found in the Ti6Al4V section. The XRD pattern of the bimetallic structure with Nb interlayer confirmed the formation of the Al_3Nb phase. Based on **Fig. 14b-vi and vii**, a reaction layer composed of $TiAl_3$ with a thickness of ~ 20 μm was formed at the interface of the bimetallic structure without Nb interlayer.

Onuike et al. [44] fabricated a Ti6Al4V/SS410 bimetallic structure with an Nb bond layer via powder-based DED technology. The processing parameters used for Ti6Al4V were 375 W laser power, 0.3-0.4 m/min laser scan speed, and 200 μm layer thickness. After the Ti6Al4V was

fully deposited, 3 layers of Nb were deposited on top of the Ti6Al4V with a laser power of 450 W, a scan speed of 0.3-0.4 m/min, and layer thickness of 150 μm. Finally, the SS410 section was deposited on top of the Nb layer with 375 W laser power, 0.3-0.4 scan speed, and 200 μm layer thickness. **Fig. 15a** shows the microstructures in each section. Unmelted Nb particles could be found within the bond layer due to insufficient energy input. A mixing zone composed of SS410 and Nb could be seen on top of the Nb layer. Dendritic microstructures were seen growing into the SS410 region, which was most likely FeNb intermetallic phases. Micro pores were also found at the interface between Nb and SS410. However, no significant cracks were found at the interface. The EDS mappings (**Fig. 15b**) show diffusions, such as Ti and V upwards into Nb and Nb into SS410. The diffusion of Nb into SS410 created the Nb + SS410 "mixing zone," which was most likely composed of FeNb intermetallic. The XRD results (Fig. 15c) identified Ti, Fe, Nb, Fe-Cr, Cr5Al8, NbC, and FeNb phases. No Fe-Ti intermetallic phases were formed at the interface, which indicated the Nb bond layer was a diffusion barrier [44].

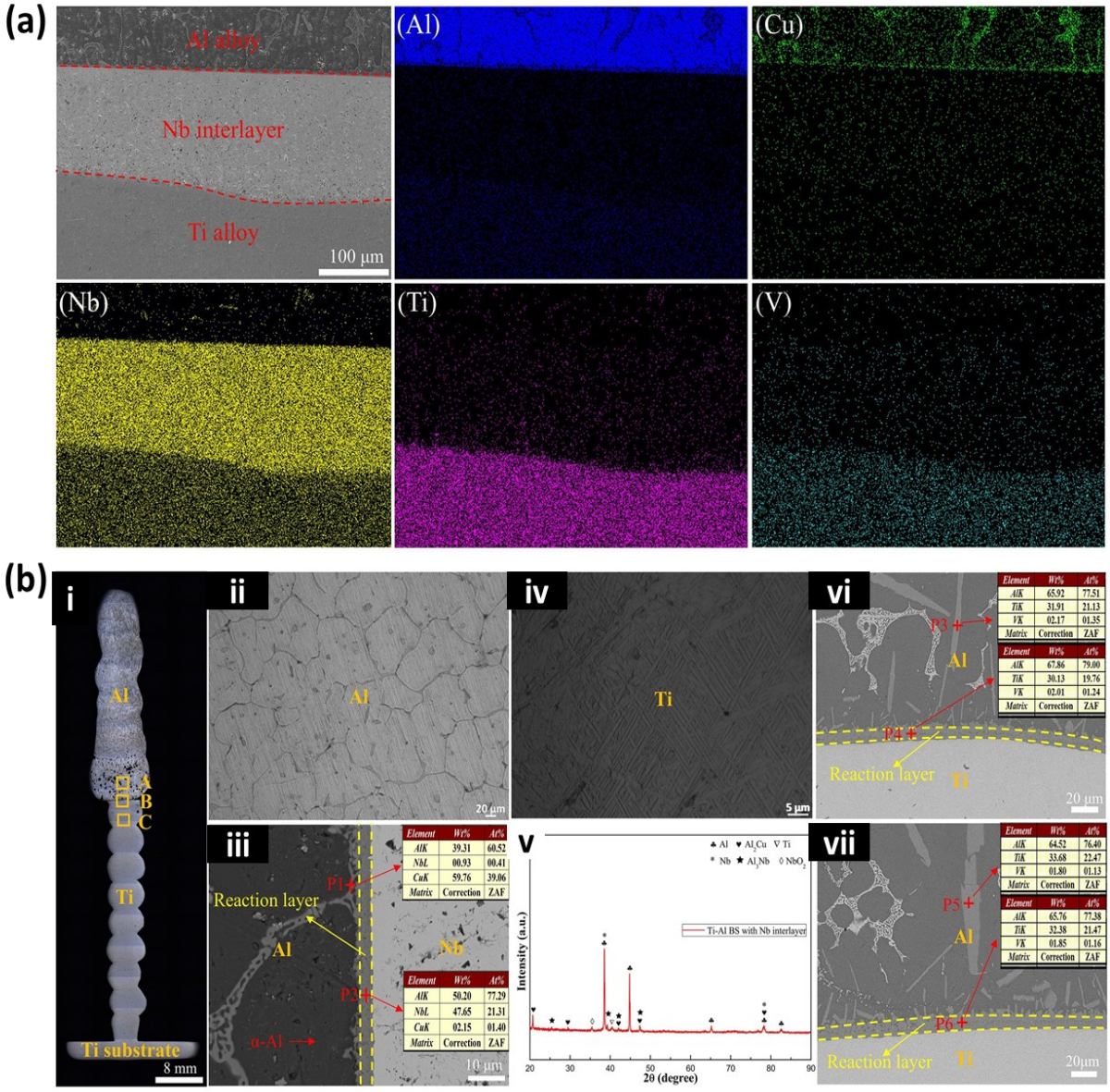

Figure 14. (a) EDS mappings of the WAAM made Ti/Al bimetallic structure with Nb bond layer. (b) Images of microstructures in each section and XRD results: (i) cross-section image of the bimetallic structure with Nb interlayer, (ii-iv) microstructures of area A-C, (v) XRD results at the interface with Nb interlayer, (vi-vii) Microstructures at the interface of the bimetallic structure without Nb interlayer [151].

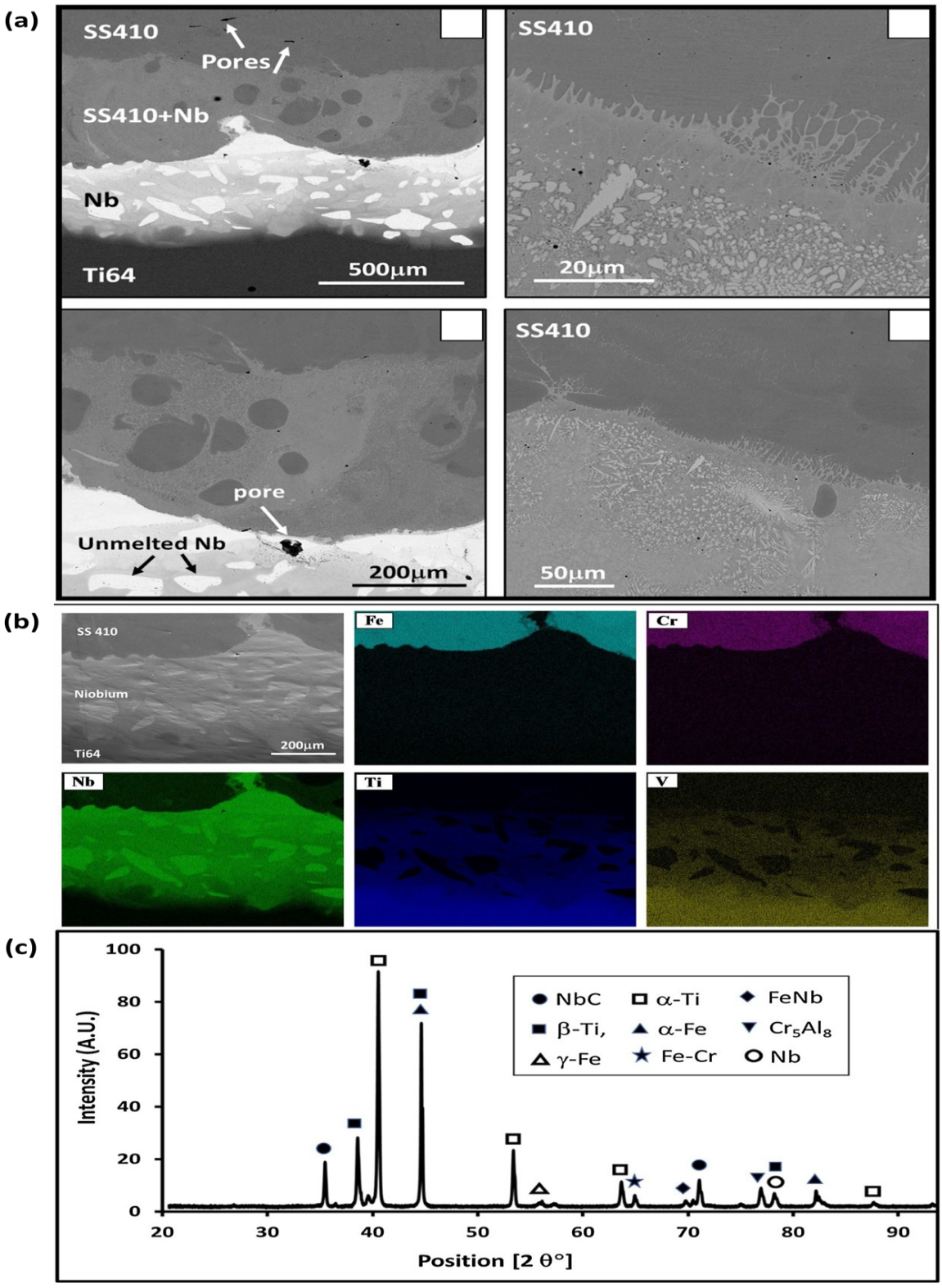

Figure 15. (a) SEM images of the Powder-based DED fabricated Ti6Al4V/SS410 bimetallic structure with Nb bond layer. (b and c) EDS mapping and XRD results at the interface [44].

7.0 Characterization of Bimetallic Structures

All characterizations performed on single material structures can potentially be performed on bimetallic structures to ascertain structural integrity alongside other desired properties, such as mechanical and thermal properties and reliability. The most common methods are physical, mechanical, and thermal characterization, including durability, as illustrated in **Fig. 16**. While other characterizations are essential, more emphasis is laid on the bimetallic joint's bond strength as it potentially affects the joint's structural integrity, including the strength and reliability of the entire structure. Although all characterization techniques are beyond this review article's scope, only essential characterization techniques for bimetallic structures are discussed here. This aspect of characterization is discussed in detail in the section below.

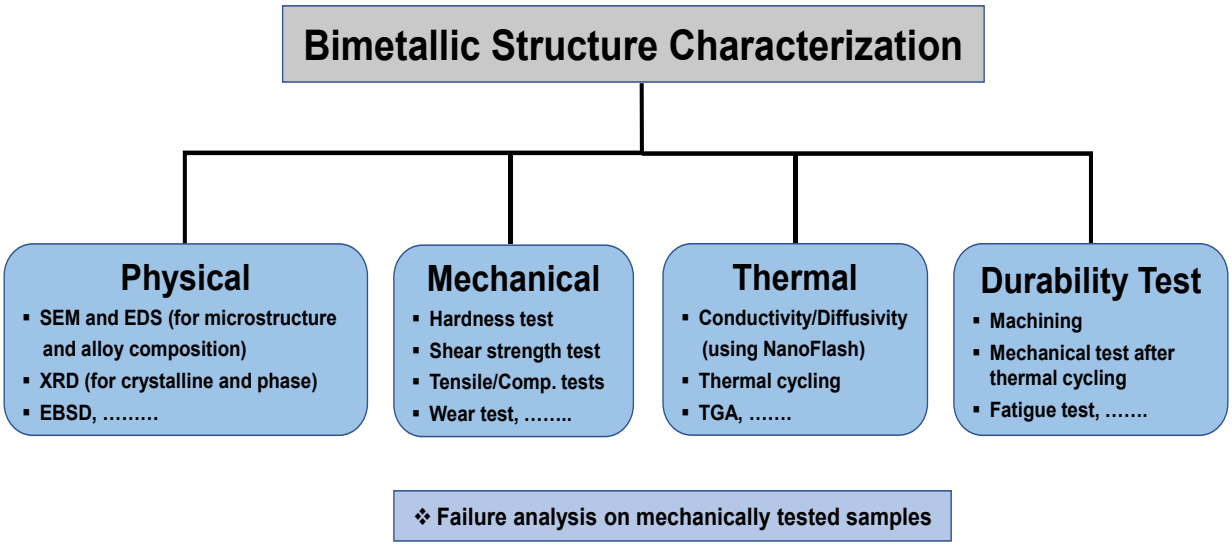

Figure 16. Methods of characterizing bimetallic structure.

7.1 Physical Characterization

The first examination conducted on any bimetallic joint, just as on single material structures, after AM processing in the as-printed condition is surface morphology via visual inspection for apparent cracks/delamination and overall build integrity. The microscope is used for a detailed examination of interfacial microcracks, while scanning electron microscopy (SEM)

reveals microstructures across the bond region. SEM examination on the bimetallic joints interface is critical for many reasons. SEM produces high-resolution images for crack identification and general topographical information. Energy dispersive spectroscopy (EDS) in the SEM reveals patterns of materials' diffusion and grain structures, while the electron backscatter diffraction (EBSD) offers preferred orientation, indicating the direction of the heat source around the bond region. **Figs. (6 to 8)** showed compound microscope and SEM images of the different bimetallic joint interfaces. Microcracks, including porosities, were revealed on titanium alloy/stainless steel joint [95,102], functionally graded TA15 to Inconel718 material [124], Inconel-steel multilayers structure [105], and other numerous samples in literature, especially the first generation experiments involving immiscible dissimilar metals processing [152–156]. The samples' defects indicate unsatisfactory product results, requiring further optimization to eliminate such features and produce a crack-free dense part.

The EDS analysis is essential to examine the extent of elemental diffusion within the bimetallic joint's mixing zone and effectively examine the extent within the bimetallic joint's mixing zone. Several EDS dots maps performed on various bimetallic joint interfaces have been reported, including the Inconel 718/GRCop-84 interface to improve Ni and Cu diffusion across the bond region [43]. The EDS line scan shows the depth of such diffusion into the base metals. A similar EDS dot map on Inconel 718/Ti64 bimetallic interfacial region shows the diffusion of various elements, especially Ti and Ni, within the CBL without getting into the base alloys [13]. This phenomenon illustrates the action of CBL as a diffusion barrier layer while stabilizing reaction products within the bond region. Other EDS maps and line-scans on various Ti or Ti-alloy to stainless steel bimetallic joins' interfaces show Fe and Ti's diffusion within the bond region [44,157]. With IBL, diffusion into base metals is hindered, and the formation of brittle intermetallic phases [44,102,116–124] is prevented. In principle, by measuring the depth of elemental diffusion within the bond region, helpful information could be obtained to quantify the bimetallic joint's interfacial bond strength via modeling. By intuition, simple diffusion will result in low bond strength, essentially due to weak metallurgical bonding.

On the other hand, X-ray diffraction (XRD) identifies different phases formed within the bond region. This analysis is essential when specific phases for good bond strength are expected. Secondly, XRD analysis helps identify the presence of any detrimental brittle intermetallic phases responsible for debonding features [13,44]. On the other hand, bimetallic joints involving

magnetic and non-magnetic materials require magnetic functionality tests, such as magnetic flux distribution around the joint region. Depending on the application area, magnetic hysteresis loss can also be conducted. Heer et al. [158] conducted a magnetic flux distribution test on the bimetallic joint of SS316/SS430 materials. The result shows a cluster of magnetized particulate materials around the SS430 section of the bimetallic joint, while the SS316 section, which is non-magnetic, was free of magnetized particulate materials. This indicates no loss of SS430 magnetic property after laser processing.

7.2 Mechanical Characterization

Primarily, mechanical characterization involves hardness tests and bond strength measurement [109,159,160], including wear tests, among others. Hardness profile across the bimetallic structure's bond region is usually performed to evaluate materials' properties variation at the region. This is important to ascertain uniform hardness distribution across the interface, influencing the joint's strength reliability and structural performance. A bimetallic joint of Inconel 718/GRCop-84 bimetallic joint processed via direct bonding and compositional gradation approaches exhibited different hardness profiles across the bond region. While the directly bonded sample showed a sharp hardness gradient, the compositionally graded sample showed gradual hardness transitioning [43]. A sharp hardness gradient at the interfacial region suggests superficial bonding, including strain localization, making the joint failure-prone. In another instance, bimetallic joints of Ti/Ti-alloy and stainless-steel materials with Nb interlayer were processed through different methods like diffusion bonding [122]. LENS process [44] showed different hardness values at the bond region. Here, the microhardness value at SS/Nb interface for diffusion bonded structure was 8.3MPa, while the microhardness value at the same region for LENS processed structure was 5.1MPa. A similar trend was observed at the Ti-Nb interface. This illustrates the impact of the processing method on hardness distribution across the bimetallic joint's interface. Also, the spike in microhardness value at the bond region could be attributed to the concentration of brittle intermetallic phases [96,161,162].

Bimetallic joint's bond strength measurement can be performed via tensile, compressive, and shear test methods for yield/ultimate strength, including elastic/shear modulus of the structure. **Fig. 17** shows tensile and shear strengths test methods/devices used on various bimetallic joints. In tensile testing, it is expected that the bimetallic joint's failure occurs at the

bond region [96], as shown in **Fig 17a**. Failures often occur further away from the interfacial joint, **Fig 17b** [163], especially on a soft material's section of the bimetallic joint. Although such a phenomenon signifies good joint strength, the exact value of the interfacial bond strength is still unknown. Similar failure behavior has been observed in the compression test method where the softer material failed by crushing [43]. Therefore, using the tensile/compression test method to evaluate bimetallic joint's bond strength requires the base materials' tensile strengths to be relatively close to each other, or the bimetallic joints' bond strength (in tensile) is low compared to the base materials. Another important compression test method evaluates the bimetallic joint's interfacial deformation behaviors, such as crack propagation and 'resistance to failure' at the joint [43,44].

While tensile/compression test methods may induce failure at undesirable sections of the bimetallic joint, the shear test method specifically evaluates interfacial bond strength at a plane of interest without base materials interaction. The lap-joint test method, described according to the ASTM D1002-99 standard, has been utilized for various shear strength measurements. However, such measurement is mostly for bond/shear strength of various adhesives/glues on metal and is not suitable for high shear strength in solidified metal-to-metal bonding [50]. The reason is that bending, necking, or tearing features occur on the base material's section close to the bond region **(Figs. 17c and d)** [97,164].

A different shear test technique is considered to accurately evaluate bimetallic interfacial joint strength to mitigate the lap joints testing method's issues. While the double shear test method is simple and produces pure shear, such a test is commonly applied to a single material structure and not suitable for bimetallic joints due to simultaneous shearing of two sections – the interface and another undesirable section to an erroneous result. Meanwhile, single-shear processes using conventionally designed devices, like the configuration utilized by Park et al. [165], introduce bending stress on the material structure and results in an impure shear at the plane of interest. Likewise, a modified version of such a device developed by Pouranvari et al. [166], shown in **Fig. 17e**, to mitigate bending stresses 'practically' introduces excess shear force that could compromise accurate measurement of shear strength.

To ensure the bimetallic joint's bond shear strength accurately, Onuike et al. [50] developed a novel single shear test device. Unique features like roller-plates and adjustable endplate, including extensometer, as shown in **Fig. 17f**, were incorporated into the device to

enhance its performance/reliability further. After fabrication, the device was calibrated and standardized with single-material metal rods. Subsequently, various bimetallic joint shear strengths, such as Inconel 718/GRCop-84, Ti64/SS410, were measured, and the results were compared with base materials. Results obtained were comparable with published data in the literature for various materials tested. Such improvement in the design of a single shear test device provides the opportunity to effectively measure bimetallic joint's bond strength of various materials' combination with good tolerance, accuracy, and repeatability.

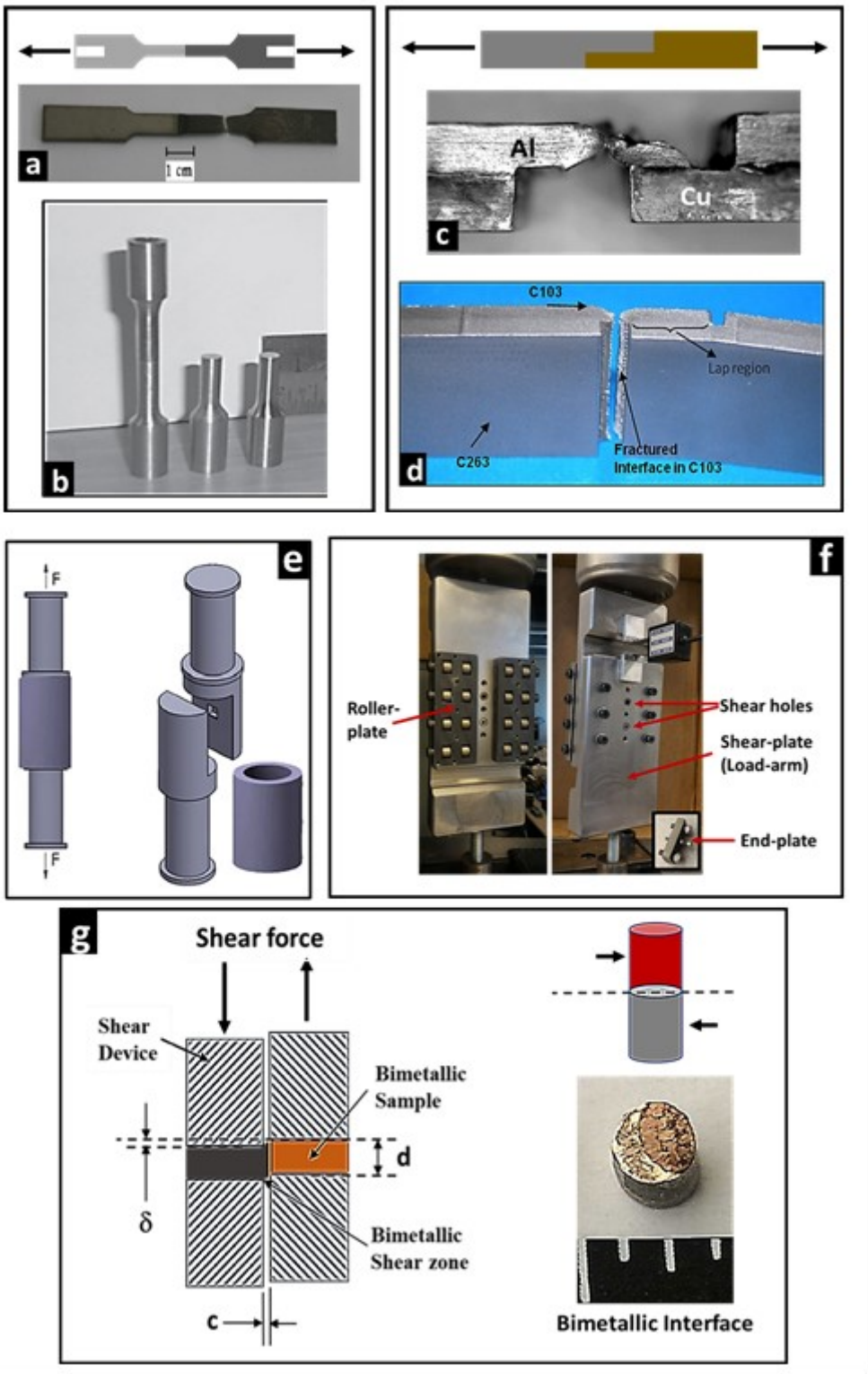

Figure 17. Bimetallic joint bond-strength test methods: (a) and (b) Tensile strength test method [96,163], (c) and(d) Lap-joint shear strength test method [97,164], (e) Sleeve-tube shear device [166], (f)and (g) Roller-plate single shear test device and bimetallic joint [50].

Table 2. Mechanical Properties of Bimetallic Structures

Conventional Process				
Process	Material Composition	Properties		
EB Welding	Ti-alloy/SS316	UTS	350 MPa	[119]
Diffusion Bonding	Ti64/304	Tensile Strength	242 MPa	[163]
	Ti/SS304 (Nb interlayer)	Tensile Strength	297 MPa	[122]
		Shear strength	217 MPa	
Brazing (Infrared)	Ti/SS (Ag interlayer)	Tensile Strength	410 MPa	[123]
AM - Process				
Process	Material Composition	Properties		
DED (LENS processed)	Inconel718/GRCop-84	Interfacial Shear Strength	220 MPa	[50]
		Compressive Y-Strength	232 MPa	
	Ti6AL4V/SS410 (Nb bond layer)	Interfacial Shear Strength	419 MPa	[44]
		Compressive Y-Strength	560 MPa	
Hybrid (Powder DED and thermal milling)	Inconel/Steel	UTS	516 MPa	[66]
DMD	Cu/H13 tool steel	Bond Strength	673 MPa	[47]
		Fracture Toughness	162 MPa/$m^{1/2}$	
Powder Bed Fusion	Maraging steel/H13	UTS (as fabricated)	664 MPa	[76]
		UTS (aged)	666 MPa	
WAAM	Steel/Nickel	Average Tensile Strength	634 MPa	[58]

7.3 Thermal Characterization

While bimetallic materials have a wide range of applications, such as in high strength/temperature regions and microelectronics, sometimes it becomes necessary to perform thermal analysis on the structural performance/reliability of the bimetallic samples. As an essential thermophysical material parameter, thermal conductivity or diffusivity describes a component's heat transport properties. Several thermal analysis testing techniques have been developed based on fundamental heat flow principles to investigate materials' thermal responses for application needs. The Netzsch NanoFlash® (LFA 447, Germany) thermal conductivity/diffusivity measurement system is one such device. It uses laser flash analysis (LFA) to measure materials' thermophysical properties [167]. In an experiment conducted using

the system to measure thermal properties of Inconel 718/GRCop-84 bimetallic joint, results showed that both the thermal diffusivity and conductivity of Inconel 718 were increased by over 200% [43] with deposition of GRCop-84. Such an increase in thermal conductivity can potentially increase operating temperatures and improve efficiency. Measurement of systems-level thermal properties is more complicated and is typically tailored for a specific device, which is certainly beyond the scope of this review.

Additionally, for a bimetallic part that undergoes high temperature to cryogenic temperature variation, thermal cycling analysis is also essential to evaluate the effect of thermal degradation on the interfacial joint as a function of temperature variations. Such a test can be conducted via a heating-hold-cooling cycle for several hours/days in a controlled heating chamber. Subsequently, interfacial microstructures and bond strength can be evaluated and compared with the as-printed sample. Further details of such testing methodology are beyond the scope of this review. Material's thermal stability for constant high-temperature applications can easily be performed via thermogravimetric analysis (TGA) through continuous measurement of mass change (oxidative mass losses) over time with temperature change under different application environments. Negligible mass loss indicates higher thermal stability of the structure. Beyond thermal stability and thermal conductivity, phase and microstructural changes due to exposure to high temperature can also be tested for the reliability of any bimetallic structures.

A durability test is crucial to measure a bimetallic joint's structural resilience and mechanical reliability. Besides maintaining dimensional accuracy, machining operations performed on bimetallic samples are the primary aspects of evaluating the joint's resistance to machining forces. Under service conditions, bimetallic samples undergo different stress cycles, such as mechanical and/or thermal. Hence, a fatigue test is essential to predict endurance limit, including the structure's performance/reliability measure even after thermal cycling. Failure analysis on the mechanically tested samples provides even more helpful information on the bimetallic joint's failure patterns/behaviors [43,44,96,119]. This can be evaluated by examining the fractography of the fractured/failed samples under shear tests, including tensile and compressive tests. The samples' deformation behaviors can provide helpful information on internal defects’ influence on the bond strength and fractographic examination of the bimetallic joint. Such results could answer many questions concerning the bimetallic joint's low bond

strength, including process optimization options for better product development and parts reliability.

8.0 Summary and future direction

It is exhilarating to see that various metal AM technologies have successfully manufactured different bimetallic structures with unique properties. Compared to traditional manufacturing methods, the reported studies have proved the feasibility and advantages of using metal AM technologies to fabricate bimetallic structures. Using various build strategies, a bimetallic structure could be printed with a compositionally graded transition that is impossible to fabricate with welding techniques. Such compositionally graded transition is significant for joining two dissimilar metallic materials, which could avoid or minimize the mismatch of the thermal properties of the two metals. In addition, AM technologies inherently allow printing structures with complex shapes. This advantage could reduce the time-cost of the processing and avoid unwanted damages during post-process machining. Current metal AM technologies provide the control of multiple processing parameters such as the energy input, feed rate of the feedstock materials, and scan speed, which let the user fabricate user-defined features and manipulate the properties of the fabricated bimetallic structures. DED-based AM machines are equipped with multiple feeders for different feedstock materials, making bimetallic structure fabrication easier and enabling *in situ* mixing to create a smooth transition between the two metallic materials.

Although using metal AM technologies to fabricate bimetallic structures may have many advantages, some critical challenges still need to be overcome. The unwanted defects at the interface between the two metallic materials could lead to critical failure in real applications. Efforts need to be made to understand the correlation between the processing parameters and the various defect formation mechanisms. Furthermore, the formation of brittle intermetallic phases at the interface can weaken the bonding strength of the bimetallic structure. Applying a compositionally graded transition between the two metals may reduce the brittle intermetallic phase formation; however, further studies are still required to understand the mechanism of intermetallic phase formation with AM processing parameters and compositional variations. Another challenge of AM processed bimetallic structures is the lack of standards. As previously mentioned, the optimized parameters for processing each type of metallic material highly depend

on AM processing methods and the utilized systems. Although energy input density is generally used to correlate the quality of metal AM processed parts and the processing parameters, researchers are still debating if energy input density is a reliable term to represent AM processed materials [168]. The lack of standards impedes the employment of novel bimetallic materials in different industrial applications, even though the material's properties are well studied [169]. Additionally, since most AM processed materials require post-processing, such as heat treatment and machining, more studies are needed to understand the impacts of post-processing on bimetallic structures' mechanical and thermal properties.

Many high-end metals AM systems are equipped with advanced monitors and sensors to obtain *in situ* information for understanding phase formations and microstructure evolution. By involving machine learning and artificial intelligence technologies, numerical models with the help of *in situ* data could be established that may be used to predict the properties of the metal AM processed materials. Developing such models and databases could significantly reduce the time cost of experimenting and testing or even manipulating the AM processed materials' final properties.

9.0 Acknowledgements

The authors would like to acknowledge financial support from the National Science Foundation under the grant number NSF-CMMI 1934230.

10.0 Declaration of Interest

The authors declare no conflict of interest.

11.0 Data Availability

Data is available upon reasonable request.

12.0 References

[1] R. Nandan, T. DebRoy, H.K.D.H. Bhadeshia, Recent advances in friction-stir welding - Process, weldment structure and properties, Prog. Mater. Sci. 53 (2008) 980–1023. https://doi.org/10.1016/j.pmatsci.2008.05.001.

[2] R. Rai, A. De, H.K.D.H. Bhadeshia, T. DebRoy, Review: friction stir welding tools., Sci. Technol. Weld. Join. 16 (2011) 325–342. http://10.0.4.155/1362171811Y.0000000023.

[3] S. Mishra, T.J. Lienert, M.Q. Johnson, T. DebRoy, An experimental and theoretical study of gas tungsten arc welding of stainless steel plates with different sulfur concentrations, Acta Mater. 56 (2008) 2133–2146. https://doi.org/10.1016/j.actamat.2008.01.028.

[4] M. Velu, S. Bhat, Experimental investigations of fracture and fatigue crack growth of copper-steel joints arc welded using nickel-base filler, Mater. Des. 67 (2015) 244–260. https://doi.org/10.1016/j.matdes.2014.11.026.

[5] A. A. Fallahi, A. Shokuhfar, A. Ostovari Moghaddam, A. Abdolahzadeh, Analysis of SiC nano-powder effects on friction stir welding of dissimilar Al-Mg alloy to A316L stainless steel, J. Manuf. Process. 30 (2017) 418–430. https://doi.org/10.1016/j.jmapro.2017.09.027.

[6] G. Casalino, S. D'Ostuni, P. Guglielmi, P. Leo, M. Mortello, G. Palumbo, A. Piccininni, Mechanical and microstructure analysis of AA6061 and Ti6Al4V fiber laser butt weld, Optik (Stuttg). 148 (2017) 151–156. https://doi.org/10.1016/j.ijleo.2017.08.138.

[7] L. Liu, Y.F. Jia, F.Z. Xuan, Gradient effect in the waved interfacial layer of 304L/533B bimetallic plates induced by explosive welding, Mater. Sci. Eng. A. 704 (2017) 493–502. https://doi.org/10.1016/j.msea.2017.08.012.

[8] G. Zu, X. Sun, J. Zhang, Interfacial Bonding Mechanism and Mechanical Performance of Ti/Steel Bimetallic Clad Sheet Produced by Explosive Welding and Annealing, Xiyou Jinshu Cailiao Yu Gongcheng/Rare Met. Mater. Eng. 46 (2017) 906–911. https://doi.org/10.1016/s1875-5372(17)30120-0.

[9] J. Ning, L.J. Zhang, G. chuan Jiang, M. xia Xie, X. qing Yin, J. xun Zhang, Narrow gap multi-pass laser butt welding of explosion welded CP-Ti/Q235B bimetallic sheet by using a copper interlayer, J. Alloys Compd. 701 (2017) 587–602.

https://doi.org/10.1016/j.jallcom.2017.01.129.

[10] A. Bandyopadhyay, K.D. Traxel, S. Bose, Nature-inspired materials and structures using 3D Printing, Mater. Sci. Eng. R Reports. 145 (2021) 100609. https://doi.org/10.1016/j.mser.2021.100609.

[11] K. D. Traxel, A. Bandyopadhyay, Influence of in situ ceramic reinforcement towards tailoring titanium matrix composites using laser-based additive manufacturing, Addit. Manuf. 31 (2020) 101004. https://doi.org/10.1016/j.addma.2019.101004.

[12] Y. Zhang, A. Bandyopadhyay, Direct fabrication of compositionally graded Ti-Al 2 O 3 multi-material structures using Laser Engineered Net Shaping, Addit. Manuf. 21 (2018) 104–111. https://doi.org/10.1016/j.addma.2018.03.001.

[13] B. Onuike, A. Bandyopadhyay, Additive manufacturing of Inconel 718 – Ti6Al4V bimetallic structures, Addit. Manuf. 22 (2018) 844–851. https://doi.org/10.1016/j.addma.2018.06.025.

[14] A. Bandyopadhyay, B. Heer, Additive manufacturing of multi-material structures, Mater. Sci. Eng. R Reports. 129 (2018) 1–16. https://doi.org/10.1016/j.mser.2018.04.001.

[15] T. C. Lin, C. Cao, M. Sokoluk, L. Jiang, X. Wang, J.M. Schoenung, E.J. Lavernia, X. Li, Aluminum with dispersed nanoparticles by laser additive manufacturing, Nat. Commun. 10 (2019) 4124. https://doi.org/10.1038/s41467-019-12047-2.

[16] M. Das, K. Bhattacharya, S.A. Dittrick, C. Mandal, V.K. Balla, T.S. Sampath Kumar, A. Bandyopadhyay, I. Manna, In situ synthesized TiB-TiN reinforced Ti6Al4V alloy composite coatings: Microstructure, tribological and in-vitro biocompatibility, J. Mech. Behav. Biomed. Mater. 29 (2014) 259–271. https://doi.org/10.1016/j.jmbbm.2013.09.006.

[17] A. Reichardt, A.A. Shapiro, R. Otis, R.P. Dillon, J.P. Borgonia, B.W. McEnerney, P. Hosemann, A.M. Beese, Advances in additive manufacturing of metal-based functionally graded materials, Int. Mater. Rev. 66 (2021) 1–29. https://doi.org/10.1080/09506608.2019.1709354.

[18] C. Zhang, F. Chen, Z. Huang, M. Jia, G. Chen, Y. Ye, Y. Lin, W. Liu, B. Chen, Q. Shen, L. Zhang, E.J. Lavernia, Additive manufacturing of functionally graded materials: A review, Mater. Sci. Eng. A. 764 (2019) 138209. https://doi.org/10.1016/j.msea.2019.138209.

[19] M. Ansari, E. Jabari, E. Toyserkani, Opportunities and challenges in additive

manufacturing of functionally graded metallic materials via powder-fed laser directed energy deposition: A review, J. Mater. Process. Technol. 294 (2021) 117117. https://doi.org/10.1016/j.jmatprotec.2021.117117.

[20] L. Yan, Y. Chen, F. Liou, Additive manufacturing of functionally graded metallic materials using laser metal deposition, Addit. Manuf. 31 (2020) 100901. https://doi.org/10.1016/j.addma.2019.100901.

[21] G. H. Loh, E. Pei, D. Harrison, M.D. Monzón, An overview of functionally graded additive manufacturing, Addit. Manuf. 23 (2018) 34–44. https://doi.org/10.1016/j.addma.2018.06.023.

[22] A. Bandyopadhyay, S. Bose, Additive Manufacturing, Boca Raton: CRC Press, Boca Raton, 2016. https://doi.org/10.1201/b18893.

[23] Amit Bandyopadhyay, Kellen D. Traxel and Susmita Bose, "Nature-inspired materials and structures using 3D Printing," *Materials Science and Engineering R*, Reports 145, 100609 (2021). https://doi.org/10.1016/j.mser.2021.100609.

[24] M. Sireesha, S.K. Albert, V. Shankar, S. Sundaresan, Comparative evaluation of welding consumables for dissimilar welds between 316LN austenitic stainless steel and Alloy 800, J. Nucl. Mater. 279 (2000) 65–76. https://doi.org/10.1016/S0022-3115(99)00275-5.

[25] Amit Bandyopadhyay, Kellen D. Traxel, Melanie Lang, Michael Juhasz, Noam Eliaz, and Susmita Bose, "Alloy Design via Additive Manufacturing: Advantages, Challenges, Applications and Perspectives," *Materials Today* (2022). doi:10.1557/s43577-021-00258-2

[26] Ultrasonic modeling and experiments: an industrial case: bimetallic weld in nuclear power plant, NDT E Int. 29 (1996) 251. https://doi.org/10.1016/0963-8695(96)90638-6.

[27] X. Guo, W. Wei, Y. Xu, A. Abd El-Aty, H. Liu, H. Wang, X. Luo, J. Tao, Wall thickness distribution of Cu–Al bimetallic tube based on free bending process, Int. J. Mech. Sci. 150 (2019) 12–19. https://doi.org/10.1016/j.ijmecsci.2018.10.013.

[28] Kellen D. Traxel and Amit Bandyopadhyay, "Designing high-temperature oxidation-resistant titanium matrix composites via directed energy deposition-based additive manufacturing," *Materials & Design*, (2021). https://doi.org/10.1016/j.matdes.2021.110205

[29] Amit Bandyopadhyay, Susmita Bose, and Roger Narayan, "Translation of 3D-Printed

Materials for Medical Applications," *MRS Bulletin*, **47** (1) (2022). doi:10.1557/s43577-021-00258-2

[30] F. A. España, V.K. Balla, S. Bose, A. Bandyopadhyay, Design and fabrication of CoCrMo alloy based novel structures for load bearing implants using laser engineered net shaping, Mater. Sci. Eng. C. 30 (2010) 50–57. https://doi.org/10.1016/j.msec.2009.08.006.

[31] B. E. Carroll, R.A. Otis, J.P. Borgonia, J.O. Suh, R.P. Dillon, A.A. Shapiro, D.C. Hofmann, Z. K. Liu, A.M. Beese, Functionally graded material of 304L stainless steel and inconel 625 fabricated by directed energy deposition: Characterization and thermodynamic modeling, Acta Mater. 108 (2016) 46–54. https://doi.org/10.1016/j.actamat.2016.02.019.

[32] Z. Guo, M. Liu, X. Bian, M. Liu, J. Li, An Al-7Si alloy/cast iron bimetallic composite with super-high shear strength, J. Mater. Res. Technol. 8 (2019) 3126–3136. https://doi.org/10.1016/j.jmrt.2017.06.014.

[33] Z. Liu, R. Ma, G. Xu, W. Wang, J. Liu, Laser additive manufacturing of bimetallic structure from Ti-6Al-4V to Ti-48Al-2Cr-2Nb via vanadium interlayer, Mater. Lett. 263 (2020) 127210. https://doi.org/10.1016/j.matlet.2019.127210.

[34] P. R. Gradl, C.S. Protz, Technology advancements for channel wall nozzle manufacturing in liquid rocket engines, Acta Astronaut. 174 (2020) 148–158. https://doi.org/10.1016/j.actaastro.2020.04.067.

[35] J. SONG, B. SUN, Thermal-structural analysis of regeneratively-cooled thrust chamber wall in reusable LOX/Methane rocket engines, Chinese J. Aeronaut. 30 (2017) 1043–1053. https://doi.org/10.1016/j.cja.2017.04.007.

[36] J. R. Riccius, E.B. Zametaev, R.H. Stark, R. Schwane, FSI analysis code validation motivated geometrical scaling of rocket engine nozzles and influence to natural frequency, in: 2018 Jt. Propuls. Conf., American Institute of Aeronautics and Astronautics, 2018. https://doi.org/10.2514/6.2018-4860.

[37] V. Dhinakaran, J. Ajith, A. Fathima Yasin Fahmidha, T. Jagadeesha, T. Sathish, B. Stalin, Wire Arc Additive Manufacturing (WAAM) process of nickel based superalloys-A review, in: Mater. Today Proc., Elsevier Ltd, 2020: pp. 920–925. https://doi.org/10.1016/j.matpr.2019.08.159.

[38] V. D. Linse, H.E. Pattee, Development of explosive welding procedures to fabricate

channeled nozzle structures, (1976).

[39] J. Xu, M. Yang, H. Ma, Z. Shen, Z. Chen, Fabrication and performance studies on explosively welded CuCrZr/316L bimetallic plate applied in extreme environments, J. Mater. Res. Technol. 9 (2020) 8971–8984. https://doi.org/10.1016/j.jmrt.2020.05.115.

[40] G.H.S.F.L. Carvalho, I. Galvão, R. Mendes, R.M. Leal, A. Loureiro, Explosive welding of aluminium to stainless steel using carbon steel and niobium interlayers, J. Mater. Process. Technol. 283 (2020) 116707. https://doi.org/10.1016/j.jmatprotec.2020.116707.

[41] X. Chen, D. Inao, S. Tanaka, A. Mori, X. Li, K. Hokamoto, Explosive welding of Al alloys and high strength duplex stainless steel by controlling energetic conditions, J. Manuf. Process. 58 (2020) 1318–1333. https://doi.org/10.1016/j.jmapro.2020.09.037.

[42] Y. Mahmood, P. wan Chen, I.A. Bataev, X. Gao, Experimental and numerical investigations of interface properties of Ti6Al4V/CP-Ti/Copper composite plate prepared by explosive welding, Def. Technol. (2020). https://doi.org/10.1016/j.dt.2020.09.003.

[43] B. Onuike, B. Heer, A. Bandyopadhyay, Additive manufacturing of Inconel 718—Copper alloy bimetallic structure using laser engineered net shaping (LENS^{TM}), Addit. Manuf. 21 (2018) 133–140. https://doi.org/10.1016/j.addma.2018.02.007.

[44] B. Onuike, A. Bandyopadhyay, Functional bimetallic joints of Ti6Al4V to SS410, Addit. Manuf. 31 (2020) 100931. https://doi.org/10.1016/j.addma.2019.100931.

[45] Y. Zhang, A. Bandyopadhyay, Influence of compositionally graded interface on microstructure and compressive deformation of 316L stainless steel to Al12Si aluminum alloy bimetallic structures, ACS Appl. Mater. Interfaces. 13 (2021) 9174–9185. https://doi.org/10.1021/acsami.0c21478.

[46] A. Bandyopadhyay, Y. Zhang, S. Bose, Recent developments in metal additive manufacturing, Curr. Opin. Chem. Eng. 28 (2020) 96–104. https://doi.org/10.1016/j.coche.2020.03.001.

[47] M. K. Imran, S.H. Masood, M. Brandt, S. Bhattacharya, J. Mazumder, Direct metal deposition (DMD) of H13 tool steel on copper alloy substrate: Evaluation of mechanical properties, Mater. Sci. Eng. A. 528 (2011) 3342–3349. https://doi.org/10.1016/j.msea.2010.12.099.

[48] S. Ji, Z. Sun, W. Zhang, X. Chen, G. Xie, H. Chang, Microstructural evolution and high temperature resistance of functionally graded material Ti-6Al-4V/Inconel 718 coated by

directed energy deposition-laser, J. Alloys Compd. 848 (2020) 156255. https://doi.org/10.1016/j.jallcom.2020.156255.

[49] Y. Zhang, A. Bandyopadhyay, Direct fabrication of bimetallic Ti6Al4V+Al12Si structures via additive manufacturing, Addit. Manuf. 29 (2019) 100783. https://doi.org/10.1016/j.addma.2019.100783.

[50] B. Onuike, A. Bandyopadhyay, Bond strength measurement for additively manufactured Inconel 718- GRCop84 copper alloy bimetallic joints, Addit. Manuf. 27 (2019) 576–585. https://doi.org/10.1016/j.addma.2019.04.003.

[51] X. Zhang, L. Li, T. Pan, Y. Chen, Y. Zhang, W. Li, F. Liou, Additive manufacturing of copper-tool steel dissimilar joining: Experimental characterization and thermal modeling, Mater. Charact. 170 (2020) 110692. https://doi.org/10.1016/j.matchar.2020.110692.

[52] J. P. Kelly, J.W. Elmer, F.J. Ryerson, J.R.I. Lee, J.J. Haslam, Directed energy deposition additive manufacturing of functionally graded Al-W composites, Addit. Manuf. 39 (2021) 101845. https://doi.org/10.1016/j.addma.2021.101845.

[53] X. Zhang, C. Sun, T. Pan, A. Flood, Y. Zhang, L. Li, F. Liou, Additive manufacturing of copper – H13 tool steel bi-metallic structures via Ni-based multi-interlayer, Addit. Manuf. 36 (2020) 101474. https://doi.org/10.1016/j.addma.2020.101474.

[54] X. Zhang, T. Pan, A. Flood, Y. Chen, Y. Zhang, F. Liou, Investigation of copper/stainless steel multi-metallic materials fabricated by laser metal deposition, Mater. Sci. Eng. A. 811 (2021) 141071. https://doi.org/10.1016/j.msea.2021.141071.

[55] N. A. Rosli, M.R. Alkahari, M.F. Abdollah, S. Maidin, F.R. Ramli, Review on effect of heat input for wire arc additive manufacturing process, J. Mater. Res. Technol. 11 (2021) 2127–2145. https://doi.org/10.1016/j.jmrt.2021.02.002.

[56] J. Wang, Z. Pan, L. Wang, L. Su, K. Carpenter, J. Wang, R. Wang, H. Li, In-situ dual wire arc additive manufacturing of NiTi-coating on Ti6Al4V alloys: Microstructure characterization and mechanical properties, Surf. Coatings Technol. 386 (2020) 125439. https://doi.org/10.1016/j.surfcoat.2020.125439.

[57] T. Abe, H. Sasahara, Dissimilar metal deposition with a stainless steel and nickel-based alloy using wire and arc-based additive manufacturing, Precis. Eng. 45 (2016) 387–395. https://doi.org/10.1016/j.precisioneng.2016.03.016.

[58] B. Wu, Z. Qiu, Z. Pan, K. Carpenter, T. Wang, D. Ding, S. Van Duin, H. Li, Enhanced

interface strength in steel-nickel bimetallic component fabricated using wire arc additive manufacturing with interweaving deposition strategy, J. Mater. Sci. Technol. 52 (2020) 226–234. https://doi.org/10.1016/j.jmst.2020.04.019.

[59] M.R.U. Ahsan, A.N.M. Tanvir, G.J. Seo, B. Bates, W. Hawkins, C. Lee, P.K. Liaw, M. Noakes, A. Nycz, D.B. Kim, Heat-treatment effects on a bimetallic additively-manufactured structure (BAMS) of the low-carbon steel and austenitic-stainless steel, Addit. Manuf. 32 (2020) 101036. https://doi.org/10.1016/j.addma.2020.101036.

[60] C. Dharmendra, S. Shakerin, G.D.J. Ram, M. Mohammadi, Wire-arc additive manufacturing of nickel aluminum bronze/stainless steel hybrid parts – Interfacial characterization, prospects, and problems, Materialia. 13 (2020) 100834. https://doi.org/10.1016/j.mtla.2020.100834.

[61] V. Utyaganova, A. Filippov, S. Tarasov, N. Shamarin, D. Gurianov, A. Vorontsov, A. Chumaevskii, S. Fortuna, N. Savchenko, V. Rubtsov, E. Kolubaev, Characterization of AA7075/AA5356 gradient transition zone in an electron beam wire-feed additive manufactured sample, Mater. Charact. 172 (2021) 110867. https://doi.org/10.1016/j.matchar.2020.110867.

[62] J. M. Flynn, A. Shokrani, S.T. Newman, V. Dhokia, Hybrid additive and subtractive machine tools - Research and industrial developments, Int. J. Mach. Tools Manuf. 101 (2016) 79–101. https://doi.org/10.1016/j.ijmachtools.2015.11.007.

[63] K. P. Karunakaran, S. Suryakumar, V. Pushpa, S. Akula, Low cost integration of additive and subtractive processes for hybrid layered manufacturing, Robot. Comput. Integr. Manuf. 26 (2010) 490–499. https://doi.org/10.1016/j.rcim.2010.03.008.

[64] S. Akula, K.P. Karunakaran, Hybrid adaptive layer manufacturing: An Intelligent art of direct metal rapid tooling process, Robot. Comput. Integr. Manuf. 22 (2006) 113–123. https://doi.org/10.1016/j.rcim.2005.02.006.

[65] E. Yasa, J.P. Kruth, J. Deckers, Manufacturing by combining Selective Laser Melting and Selective Laser Erosion/laser re-melting, CIRP Ann. - Manuf. Technol. 60 (2011) 263–266. https://doi.org/10.1016/j.cirp.2011.03.063.

[66] P. Li, Y. Gong, Y. Xu, Y. Qi, Y. Sun, H. Zhang, Inconel-steel functionally bimetal materials by hybrid directed energy deposition and thermal milling: Microstructure and mechanical properties, Arch. Civ. Mech. Eng. 19 (2019) 820–831.

https://doi.org/10.1016/j.acme.2019.03.002.

[67] S. Yin, X. Yan, C. Chen, R. Jenkins, M. Liu, R. Lupoi, Hybrid additive manufacturing of Al-Ti6Al4V functionally graded materials with selective laser melting and cold spraying, J. Mater. Process. Technol. 255 (2018) 650–655. https://doi.org/10.1016/j.jmatprotec.2018.01.015.

[68] C. Y. Yap, C.K. Chua, Z.L. Dong, Z.H. Liu, D.Q. Zhang, L.E. Loh, S.L. Sing, Review of selective laser melting: Materials and applications, Appl. Phys. Rev. 2 (2015) 41101. https://doi.org/10.1063/1.4935926.

[69] J. Wang, W.J. Wu, W. Jing, X. Tan, G.J. Bi, S.B. Tor, K.F. Leong, C.K. Chua, E. Liu, Improvement of densification and microstructure of ASTM A131 EH36 steel samples additively manufactured via selective laser melting with varying laser scanning speed and hatch spacing, Mater. Sci. Eng. A. Struct. Mater. 746 (2019) 300–313. https://doi.org/10.1016/j.msea.2019.01.019.

[70] X. Tan, Y. Kok, Y.J. Tan, G. Vastola, Q.X. Pei, G. Zhang, Y.W. Zhang, S.B. Tor, K.F. Leong, C.K. Chua, An experimental and simulation study on build thickness dependent microstructure for electron beam melted Ti-6Al-4V, J. Alloys Compd. 646 (2015) 303–309. https://doi.org/10.1016/j.jallcom.2015.05.178.

[71] X. Tan, Y. Kok, Y.J. Tan, M. Descoins, D. Mangelinck, S.B. Tor, K.F. Leong, C.K. Chua, Graded microstructure and mechanical properties of additive manufactured Ti–6Al–4V via electron beam melting, Acta Mater. 97 (2015) 1–16. https://doi.org/10.1016/j.actamat.2015.06.036.

[72] J. Chen, Y. Yang, C. Song, D. Wang, S. Wu, M. Zhang, Influence mechanism of process parameters on the interfacial characterization of selective laser melting 316L/CuSn10, Mater. Sci. Eng. A. 792 (2020) 139316. https://doi.org/10.1016/j.msea.2020.139316.

[73] Z. Sun, Y-H. Chueh, L. Li (2020) Multiphase mesoscopic simulation of multiple and functionally gradient materials laser powder bed fusion additive manufacturing processes Addt Manuf, vol. 35, p. 101448

[74] L. Yao, S. Huang, U. Ramamurty, Z. M. Xiao, (2021) On the formation of “Fish-scale” morphology with curved grain interfacial microstructures during selective laser melting of dissimilar alloys Acta Materialia, vol. 220, p. 117331

[75] S. L. Sing, S. Huang, G. D. Goh, G. L. Goh, C. F. Tey, J. H. L. Tan, W. Y. Yeong (2021) Emerging metallic systems for additive manufacturing: In-situ alloying and multi-metal processing in laser powder bed fusion, Progress in Materials Science, vol. 119, p. 100795

[76] S. Shakerin, M. Sanjari, B.S. Amirkhiz, M. Mohammadi, Interface engineering of additively manufactured maraging steel-H13 bimetallic structures, Mater. Charact. 170 (2020) 110728. https://doi.org/10.1016/j.matchar.2020.110728.

[77] A. Hadadzadeh, B.S. Amirkhiz, S. Shakerin, J. Kelly, J. Li, M. Mohammadi, Microstructural investigation and mechanical behavior of a two-material component fabricated through selective laser melting of AlSi10Mg on an Al-Cu-Ni-Fe-Mg cast alloy substrate, Addit. Manuf. 31 (2020) 100937. https://doi.org/10.1016/j.addma.2019.100937.

[78] J. Chen, Y. Yang, C. Song, M. Zhang, S. Wu, D. Wang, Interfacial microstructure and mechanical properties of 316L /CuSn10 multi-material bimetallic structure fabricated by selective laser melting, Mater. Sci. Eng. A. 752 (2019) 75–85. https://doi.org/10.1016/j.msea.2019.02.097.

[79] M. Zhang, Y. Yang, D. Wang, C. Song, J. Chen, Microstructure and mechanical properties of CuSn/18Ni300 bimetallic porous structures manufactured by selective laser melting, Mater. Des. 165 (2019) 107583. https://doi.org/10.1016/j.matdes.2019.107583.

[80] S. L. Sing, L.P. Lam, D.Q. Zhang, Z.H. Liu, C.K. Chua, Interfacial characterization of SLM parts in multi-material processing: Intermetallic phase formation between AlSi10Mg and C18400 copper alloy, Mater. Charact. 107 (2015) 220–227. https://doi.org/10.1016/j.matchar.2015.07.007.

[81] X. Mei, X. Wang, Y. Peng, H. Gu, G. Zhong, S. Yang, Interfacial characterization and mechanical properties of 316L stainless steel/inconel 718 manufactured by selective laser melting, Mater. Sci. Eng. A. 758 (2019) 185–191. https://doi.org/10.1016/j.msea.2019.05.011.

[82] C. Tan, K. Zhou, T. Kuang. (2019) Selective laser melting of tungsten-copper functionally graded material, Materials Letters, vol. 237, pp. 328-331

[83] C. F Tey, X. Tan, S. L Sing, W. Y Yeong. (2020) Additive manufacturing of multiple materials by selective laser melting: Ti-alloy to stainless steel via a Cu-alloy interlayer, Additive Manufacturing, vol. 31, p. 100970.

[84] T. D Ngo, A. Kashani, G. Imbalzano, K. T. Q Nguyen, D. Hui (2018) Additive

manufacturing (3D printing): a review of materials, methods, applications and challenges. Compos Part B Eng 143:172–196. https://doi.org/10.1016/j.compositesb.2018.02.012

[85] W. E Frazier (2014) Metal additive manufacturing: a review. J Mater Eng Perform 23:1917–1928. https://doi.org/10.1007/s11665-014-0958-z

[86] Y. Huang, M. C Leu, J. Mazumder, A. Donmez (2015) Additive manufacturing: current state, future potential, gaps and needs, and recommendations. J Manuf Sci Eng Trans ASME 137:1–11. https://doi.org/10.1115/1.4028725

[87] M. K Thompson, G. Moroni, T. Vaneker, G. Fadel, R. I Campbell, I. Gibson, A. Bernard, J. Schulz, P. Graf, B. Ahuja, F. Martina (2016) Design for additive manufacturing: trends, opportunities, considerations, and constraints. CIRP Ann Manuf Technol 65: 737–760. https://doi.org/10.1016/j.cirp.2016.05.004

[88] D. Ding, Z. Pan, D. Cuiuri, H. Li (2015) Wire-feed additive manufacturing of metal components: technologies, developments and future interests Int. J. Adv. Manuf. Technol. 81 465–481.

[89] C. Wei and L. Li, "Recent progress and scientific challenges in multi-material additive manufacturing via laser-based powder bed fusion," Virtual and Physical Prototyping, pp. 1-25, 2021.

[90] B. Ahuja, M. Karg, M. Schmidt (2015) Additive manufacturing in production: challenges and opportunities. Laser 3D Manuf II 9353:935304. https://doi.org/10.1117/12.2082521

[91] J. Schmelzle, E. V Kline, C. J Dickman, E. W Reutzel, G. Jones, T. W Simpson (2015) (Re) Designing for part consolidation: understanding the challenges of metal additive manufacturing. J Mech Des Trans ASME 137:1–12. https://doi.org/10.1115/1.4031156

[92] F. Liou, K. Slattery, M. Kinsella, J. Newkirk, H.N Chou, R. Landers (2007) Applications of a hybrid manufacturing process for fabrication of metallic structures. Rapid Prototyp J 13:236–244. https://doi.org/10.1108/13552540710776188.

[93] W. Du, Q. Bai, B. Zhang (2016) A novel method for additive/subtractive hybrid manufacturing of metallic parts. Procedia Manuf 5:1018–1030. https://doi.org/10.1016/j.promfg.2016.08.067.

[94] A. Jiménez, P. Bidare, H. Hassanin, F. Tarlochan, S. Dimov, K. Essa (2021) Powder-based laser hybrid additive manufacturing of metals: a review. Int. J. Adv. Manuf. Technol 114:63–96

[95] S. Chen, M. Zhang, J. Huang, C. Cui, H. Zhang, X. Zhao, Microstructures and mechanical property of laser butt welding of titanium alloy to stainless steel, Mater. Des. 53 (2014) 504–511. https://doi.org/10.1016/j.matdes.2013.07.044.

[96] S. Kundu, S. Sam, S. Chatterjee, Interface microstructure and strength properties of Ti-6Al-4V and microduplex stainless steel diffusion bonded joints, Mater. Des. 32 (2011) 2997–3003. https://doi.org/10.1016/j.matdes.2010.12.052.

[97] P. Mastanaiah, G. Madhusudhan Reddy, K. Satya Prasad, C.V.S. Murthy, An investigation on microstructures and mechanical properties of explosive cladded C103 niobium alloy over C263 nimonic alloy, J. Mater. Process. Technol. 214 (2014) 2316–2324. https://doi.org/10.1016/j.jmatprotec.2014.04.025.

[98] Q. Z. Zhang, W.B. Gong, W. Liu, Microstructure and mechanical properties of dissimilar Al-Cu joints by friction stir welding, Trans. Nonferrous Met. Soc. China (English Ed. 25 (2015) 1779–1786. https://doi.org/10.1016/S1003-6326(15)63783-9.

[99] H. C. Chen, A.J. Pinkerton, L. Li, Fibre laser welding of dissimilar alloys of Ti-6Al-4V and Inconel 718 for aerospace applications, Int. J. Adv. Manuf. Technol. 52 (2011) 977–987. https://doi.org/10.1007/s00170-010-2791-3.

[100] K. Shah, I.U. Haq, S.A. Shah, F.U. Khan, M.T. Khan, S. Khan, Experimental study of direct laser deposition of ti-6al-4v and inconel 718 by using pulsed parameters, Sci. World J. 2014 (2014) 841546–841549. https://doi.org/10.1155/2014/841549.

[101] C. Shang, C. Wang, C. Li, G. Yang, G. Xu, J. You, Eliminating the crack of laser 3D printed functionally graded material from TA15 to Inconel718 by base preheating, Opt. Laser Technol. 126 (2020) 106100. https://doi.org/10.1016/j.optlastec.2020.106100.

[102] H. Sahasrabudhe, R. Harrison, C. Carpenter, A. Bandyopadhyay, Stainless steel to titanium bimetallic structure using LENS^{TM}, Addit. Manuf. 5 (2015) 1–8. https://doi.org/10.1016/j.addma.2014.10.002.

[103] S. Tammas-Williams, I. Todd, R.M. Mahamood, E.T. Akinlabi, S. Tammas-Williams, I. Todd, Functionally graded materials, Cham: Springer International Publishing AG, Cham, 2017. https://doi.org/10.1201/9781315151441.

[104] D. C. Hofmann, J. Kolodziejska, S. Roberts, R. Otis, R.P. Dillon, J.O. Suh, Z.K. Liu, J.P. Borgonia, Compositionally graded metals: A new frontier of additive manufacturing, J. Mater. Res. 29 (2014) 1899–1910. https://doi.org/10.1557/jmr.2014.208.

[105] S. C. Bodner, L.T.G. van de Vorst, J. Zalesak, J. Todt, J.F. Keckes, V. Maier-Kiener, B. Sartory, N. Schell, J.W. Hooijmans, J.J. Saurwalt, J. Keckes, Inconel-steel multilayers by liquid dispersed metal powder bed fusion: Microstructure, residual stress and property gradients, Addit. Manuf. 32 (2020) 101027. https://doi.org/10.1016/j.addma.2019.101027.

[106] M. S. Domack, J.M. Baughman, Development of nickel-titanium graded composition components, Rapid Prototyp. J. 11 (2005) 41–51. https://doi.org/10.1108/13552540510573383.

[107] R. Martinez, I. Todd, K. Mumtaz (2019) In situ alloying of elemental Al-Cu12 feedstock using selective laser melting, Virtual and Physical Prototyping, vol. 14, (3) pp. 242-252.

[108] A. Reichardt, R.P. Dillon, J.P. Borgonia, A.A. Shapiro, B.W. McEnerney, T. Momose, P. Hosemann, Development and characterization of Ti-6Al-4V to 304L stainless steel gradient components fabricated with laser deposition additive manufacturing, Mater. Des. 104 (2016) 404–413. https://doi.org/10.1016/j.matdes.2016.05.016.

[109] L. D. Bobbio, R.A. Otis, J.P. Borgonia, R.P. Dillon, A.A. Shapiro, Z.K. Liu, A.M. Beese, Additive manufacturing of a functionally graded material from Ti-6Al-4V to Invar: Experimental characterization and thermodynamic calculations, Acta Mater. 127 (2017) 133–142. https://doi.org/10.1016/j.actamat.2016.12.070.

[110] F. Otto, Y. Yang, H. Bei, E.P. George, Relative effects of enthalpy and entropy on the phase stability of equiatomic high-entropy alloys, Acta Mater. 61 (2013) 2628–2638. https://doi.org/10.1016/j.actamat.2013.01.042.

[111] J.W. Yeh, S.K. Chen, S.J. Lin, J.Y. Gan, T.S. Chin, T.T. Shun, C.H. Tsau, S.Y. Chang, Nanostructured high-entropy alloys with multiple principal elements: Novel alloy design concepts and outcomes, Adv. Eng. Mater. 6 (2004) 299–303. https://doi.org/10.1002/adem.200300567.

[112] W. Hume-Rothery, Atomic diameters, atomic volumes and solid solubility relations in alloys, Acta Metall. 14 (1966) 17–20. https://doi.org/10.1016/0001-6160(66)90267-7.

[113] Y. Zhang, Y.J. Zhou, J.P. Lin, G.L. Chen, P.K. Liaw, Solid-solution phase formation rules for multi-component alloys, Adv. Eng. Mater. 10 (2008) 534–538. https://doi.org/10.1002/adem.200700240.

[114] Z. Wang, Y. Huang, Y. Yang, J. Wang, C.T. Liu, Atomic-size effect and solid solubility of multicomponent alloys, Scr. Mater. 94 (2015) 28–31.

https://doi.org/10.1016/j.scriptamat.2014.09.010.

[115] The Materials Information Society, ASM Handbook Volume 3 - Alloy Phase Diagrams, ASM International, 1992. https://doi.org/10.1007/BF02869318.

[116] S. Kundu, S. Chatterjee, D. Olson, B. Mishra, Effects of intermetallic phases on the bond strength of diffusion-bonded joints between titanium and 304 stainless steel using nickel interlayer, Metall. Mater. Trans. A Phys. Metall. Mater. Sci. 38 A (2007) 2053–2060. https://doi.org/10.1007/s11661-007-9273-8.

[117] S. Kundu, S. Chatterjee, Interfacial microstructure and mechanical properties of diffusion-bonded titanium-stainless steel joints using a nickel interlayer, Mater. Sci. Eng. A. 425 (2006) 107–113. https://doi.org/10.1016/j.msea.2006.03.034.

[118] S. Kundu, M. Ghosh, A. Laik, K. Bhanumurthy, G.B. Kale, S. Chatterjee, Diffusion bonding of commercially pure titanium to 304 stainless steel using copper interlayer, Mater. Sci. Eng. A. 407 (2005) 154–160. https://doi.org/10.1016/j.msea.2005.07.010.

[119] I. Tomashchuk, P. Sallamand, N. Belyavina, M. Pilloz, Evolution of microstructures and mechanical properties during dissimilar electron beam welding of titanium alloy to stainless steel via copper interlayer, Mater. Sci. Eng. A. 585 (2013) 114–122. https://doi.org/10.1016/j.msea.2013.07.050.

[120] A. Elrefaey, W. Tillmann, Solid state diffusion bonding of titanium to steel using a copper base alloy as interlayer, J. Mater. Process. Technol. 209 (2009) 2746–2752. https://doi.org/10.1016/j.jmatprotec.2008.06.014.

[121] M. Balasubramanian, Characterization of diffusion-bonded titanium alloy and 304 stainless steel with Ag as an interlayer, Int. J. Adv. Manuf. Technol. 82 (2016) 153–162. https://doi.org/10.1007/s00170-015-7376-8.

[122] S. Kundu, S. Chatterjee, Evolution of interface microstructure and mechanical properties of titanium/304 stainless steel diffusion bonded joint using Nb interlayer, ISIJ Int. 50 (2010) 1460–1465. https://doi.org/10.2355/isijinternational.50.1460.

[123] J. G. Lee, S.J. Hong, M.K. Lee, C.K. Rhee, High strength bonding of titanium to stainless steel using an Ag interlayer, J. Nucl. Mater. 395 (2009) 145–149. https://doi.org/10.1016/j.jnucmat.2009.10.045.

[124] C. Shang, C. Wang, G. Xu, C. Li, J. You, Laser additive manufacturing of TA15 - Inconel 718 bimetallic structure via Nb/Cu multi-interlayer, Vacuum. 169 (2019) 108888.

https://doi.org/10.1016/j.vacuum.2019.108888.

[125] R. K. Shiue, S.K. Wu, J.Y. Shiue, Infrared brazing of Ti-6Al-4V and 17-4 PH stainless steel with (Ni)/Cr barrier layer(s), Mater. Sci. Eng. A. 488 (2008) 186–194. https://doi.org/10.1016/j.msea.2007.10.075.

[126] P. Li, J. Li, J. Xiong, F. Zhang, S.H. Raza, Diffusion bonding titanium to stainless steel using Nb/Cu/Ni multi-interlayer, Mater. Charact. 68 (2012) 82–87. https://doi.org/10.1016/j.matchar.2012.03.016.

[127] S. Hasanov, S. Alkunte, M. Rajeshirke, A. Gupta, O. Huseynov, I. Fidan, F. Alifui-Segbaya, A. Rennie, (2022) Review on additive manufacturing of multi-material parts: progress and challenges. J. Manuf. Mater. Process. 6, 4. https://doi.org/10.3390/jmmp6010004

[128] I. Mitra, S. Bose, W.S. Dernell, N. Dasgupta, C. Eckstrand, J. Herrick, M.J. Yaszemski, S.B. Goodman, A. Bandyopadhyay, 3D Printing in alloy design to improve biocompatibility in metallic implants, Mater. Today. (2021). https://doi.org/10.1016/j.mattod.2020.11.021.

[129] V. K. Balla, S. Banerjee, S. Bose, A. Bandyopadhyay, Direct laser processing of a tantalum coating on titanium for bone replacement structures, Acta Biomater. 6 (2010) 2329–2334. https://doi.org/10.1016/j.actbio.2009.11.021.

[130] J. Ju, Y. Zhou, K. Wang, Y. Liu, J. Li, M. Kang, J. Wang, Tribological investigation of additive manufacturing medical Ti6Al4V alloys against Al2O3 ceramic balls in artificial saliva, J. Mech. Behav. Biomed. Mater. 104 (2020) 103602. https://doi.org/10.1016/j.jmbbm.2019.103602.

[131] L. Denti, E. Bassoli, A. Gatto, E. Santecchia, P. Mengucci, Fatigue life and microstructure of additive manufactured Ti6Al4V after different finishing processes, Mater. Sci. Eng. A. 755 (2019) 1–9. https://doi.org/10.1016/j.msea.2019.03.119.

[132] G. Kasperovich, J. Hausmann, Improvement of fatigue resistance and ductility of TiAl6V4 processed by selective laser melting, J. Mater. Process. Technol. 220 (2015) 202–214. https://doi.org/10.1016/j.jmatprotec.2015.01.025.

[133] A. Bandyopadhyay, M. Upadhyayula, K.D. Traxel, B. Onuike, Influence of deposition orientation on fatigue response of LENS^{TM} processed Ti6Al4V, Mater. Lett. 255 (2019) 126541. https://doi.org/10.1016/j.matlet.2019.126541.

[134] M. Simonelli, Y.Y. Tse, C. Tuck, On the texture formation of selective laser melted Ti-6Al-4V, Metall. Mater. Trans. A Phys. Metall. Mater. Sci. 45 (2014) 2863–2872. https://doi.org/10.1007/s11661-014-2218-0.

[135] A. Mertens, S. Reginster, H. Paydas, Q. Contrepois, T. Dormal, O. Lemaire, J. Lecomte-Beckers, Mechanical properties of alloy Ti-6Al-4V and of stainless steel 316L processed by selective laser melting: influence of out-of-equilibrium microstructures., Powder Metall. 57 (2014) 184–189. http://10.0.4.155/1743290114Y.0000000092.

[136] S. Liu, K.M. Hong, C. Katinas, Y.C. Shin, Multiphysics modeling of phase transformation and microhardness evolution in laser direct deposited Ti6Al4V, J. Manuf. Process. 45 (2019) 579–587. https://doi.org/10.1016/j.jmapro.2019.07.027.

[137] M. Buciumeanu, A. Bagheri, N. Shamsaei, S.M. Thompson, F.S. Silva, B. Henriques, Tribocorrosion behavior of additive manufactured Ti-6Al-4V biomedical alloy, Tribol. Int. 119 (2018) 381–388. https://doi.org/10.1016/j.triboint.2017.11.032.

[138] A. Xue, X. Lin, L. Wang, J. Wang, W. Huang, Influence of trace boron addition on microstructure, tensile properties and their anisotropy of Ti6Al4V fabricated by laser directed energy deposition, Mater. Des. 181 (2019) 107943. https://doi.org/10.1016/j.matdes.2019.107943.

[139] G. Bonaiti, P. Parenti, M. Annoni, S. Kapoor, Micro-milling Machinability of DED Additive Titanium Ti-6Al-4V, Procedia Manuf. 10 (2017) 497–509. https://doi.org/10.1016/j.promfg.2017.07.104.

[140] D. C. Hofmann, S. Roberts, R. Otis, J. Kolodziejska, R.P. Dillon, J. Suh, A.A. Shapiro, Z.-K. Liu, J.-P. Borgonia, Developing Gradient Metal Alloys through Radial Deposition Additive Manufacturing, Sci. Rep. 4 (2014) 5357. https://doi.org/10.1038/srep05357.

[141] P. C. Collins, R. Banerjee, S. Banerjee, H.L. Fraser, Laser deposition of compositionally graded titanium-vanadium and titanium-molybdenum alloys, Mater. Sci. Eng. A. 352 (2003) 118–128. https://doi.org/10.1016/S0921-5093(02)00909-7.

[142] I. Yadroitsev, P. Bertrand, I. Smurov, Parametric analysis of the selective laser melting process, Appl. Surf. Sci. 253 (2007) 8064–8069. https://doi.org/10.1016/j.apsusc.2007.02.088.

[143] A. Simchi, Direct laser sintering of metal powders: Mechanism, kinetics and microstructural features, Mater. Sci. Eng. A. 428 (2006) 148–158.

https://doi.org/10.1016/j.msea.2006.04.117.

[144] A. G. Demir, B. Previtali, Multi-material selective laser melting of Fe/Al-12Si components, Manuf. Lett. 11 (2017) 8–11. https://doi.org/10.1016/j.mfglet.2017.01.002.

[145] B. Song, S. Dong, P. Coddet, H. Liao, C. Coddet, Fabrication and microstructure characterization of selective laser-melted FeAl intermetallic parts, Surf. Coatings Technol. 206 (2012) 4704–4709. https://doi.org/10.1016/j.surfcoat.2012.05.072.

[146] Z. H. Liu, D.Q. Zhang, S.L. Sing, C.K. Chua, L.E. Loh, Interfacial characterization of SLM parts in multi-material processing: Metallurgical diffusion between 316L stainless steel and C18400 copper alloy, Mater. Charact. 94 (2014) 116–125. https://doi.org/10.1016/j.matchar.2014.05.001.

[147] M. R. U. Ahsan, X. Fan, G.J. Seo, C. Ji, M. Noakes, A. Nycz, P.K. Liaw, D.B. Kim, Microstructures and mechanical behavior of the bimetallic additively-manufactured structure (BAMS) of austenitic stainless steel and Inconel 625, J. Mater. Sci. Technol. 74 (2021) 176–188. https://doi.org/10.1016/j.jmst.2020.10.001.

[148] D. J. Kotecki, J.C. Lippold, Welding metallurgy and weldability of stainless steels, Hoboken, NJ : John Wiley, Hoboken, NJ, 2005.

[149] A. N. M. Tanvir, M.R.U. Ahsan, C. Ji, W. Hawkins, B. Bates, D.B. Kim, Heat treatment effects on Inconel 625 components fabricated by wire + arc additive manufacturing (WAAM)—part 1: microstructural characterization, Int. J. Adv. Manuf. Technol. 103 (2019) 3785–3798. https://doi.org/10.1007/s00170-019-03828-6.

[150] C. Schneider-Maunoury, L. Weiss, D. Boisselier, P. Laheurte, Crystallographic analysis of functionally graded titanium-molybdenum alloys with DED-CLAD® process, in: Procedia CIRP, Elsevier B.V., 2018: pp. 180–183. https://doi.org/10.1016/j.procir.2018.08.089.

[151] N. Xu, J. Shen, S. Hu, Y. Tian, J. Bi, Bimetallic structure of Ti6Al4V and Al6.21Cu fabricated by cold metal transfer additive manufacturing via Nb interlayer added by TIG, Mater. Lett. 302 (2021) 130397. https://doi.org/10.1016/J.MATLET.2021.130397.

[152] L. Chen, C. Wang, X. Zhang, G. Mi, Effect of parameters on microstructure and mechanical property of dissimilar joints between 316L stainless steel and GH909 alloy by laser welding, J. Manuf. Process. 65 (2021) 60–69. https://doi.org/10.1016/j.jmapro.2021.03.015.

[153] N. Jiménez Mena, T. Sapanathan, P.J. Jacques, A. Simar, Combined numerical and experimental estimation of the fracture toughness and failure analysis of single lap shear test for dissimilar welds, Eng. Fract. Mech. (2021) 107756. https://doi.org/10.1016/j.engfracmech.2021.107756.

[154] P. Singh, D. Deepak, G.S. Brar, Optical micrograph and micro-hardness behavior of dissimilar welded joints of aluminum (Al 6061-T6) and stainless steel (SS 304) with friction crush welding, Mater. Today Proc. 44 (2021) 1000–1004. https://doi.org/10.1016/j.matpr.2020.11.171.

[155] S. Li, L. Hu, P. Dai, T. Bi, D. Deng, Influence of the groove shape on welding residual stresses in P92/SUS304 dissimilar metal butt-welded joints, J. Manuf. Process. 66 (2021) 376–386. https://doi.org/10.1016/j.jmapro.2021.04.030.

[156] S. R. Naik, G.M. Gadad, A.M. Hebbale, Joining of dissimilar metals using microwave hybrid heating and Tungsten Inert Gas welding - A review, Mater. Today Proc. (2021). https://doi.org/10.1016/j.matpr.2021.02.322.

[157] K. N. Campo, L.C. Campanelli, L. Bergmann, J.F. dos Santos, C. Bolfarini, Microstructure and interface characterization of dissimilar friction stir welded lap joints between Ti-6Al-4V and AISI 304, Mater. Des. 56 (2014) 139–145. https://doi.org/10.1016/j.matdes.2013.11.002.

[158] B. Heer, A. Bandyopadhyay, Compositionally graded magnetic-nonmagnetic bimetallic structure using laser engineered net shaping, Mater. Lett. 216 (2018) 16–19. https://doi.org/10.1016/j.matlet.2017.12.129.

[159] A. E. Wilson-Heid, A.M. Beese, Combined effects of porosity and stress state on the failure behavior of laser powder bed fusion stainless steel 316L, Addit. Manuf. 39 (2021) 101862. https://doi.org/10.1016/j.addma.2021.101862.

[160] S. Qin, T. C. Novak, M.K. Vailhe, Z.K. Liu, A.M. Beese, Plasticity and fracture behavior of Inconel 625 manufactured by laser powder bed fusion: Comparison between as-built and stress relieved conditions, Mater. Sci. Eng. A. 806 (2021) 140808. https://doi.org/10.1016/j.msea.2021.140808.

[161] T. Vigraman, D. Ravindran, R. Narayanasamy, Effect of phase transformation and intermetallic compounds on the microstructure and tensile strength properties of diffusion-bonded joints between Ti-6Al-4V and AISI 304L, Mater. Des. 36 (2012) 714–727.

https://doi.org/10.1016/j.matdes.2011.12.024.

[162] N. Orhan, T. I. Khan, M. Eroğlu, Diffusion bonding of a microduplex stainless steel to Ti-6Al-4V, Scr. Mater. 45 (2001) 441–446. https://doi.org/10.1016/S1359-6462(01)01041-7.

[163] M. J. Torkamany, F. Malek Ghaini, R. Poursalehi, Dissimilar pulsed Nd: YAG laser welding of pure niobium to Ti-6Al-4V, Mater. Des. 53 (2014) 915–920. https://doi.org/10.1016/j.matdes.2013.07.094.

[164] R. Uscinowicz, Impact of temperature on shear strength of single lap Al-Cu bimetallic joint, Compos. Part B Eng. 44 (2013) 344–356. https://doi.org/10.1016/j.compositesb.2012.04.073.

[165] J. W. Park, P.F. Mendez, T.W. Eagar, Strain energy distribution in ceramic-to-metal joints, Acta Mater. 50 (2002) 883–899. https://doi.org/10.1016/S1359-6454(01)00352-4.

[166] M. Pouranvari, A. Ekrami, A.H. Kokabi, Effect of the bonding time on the microstructure and mechanical properties of a transient-liquid-phase bonded in718 using a Ni-Cr-B filler alloy, Mater. Tehnol. 47 (2013) 593–599.

[167] Thermal Diffusivity/Conductivity, Seebeck Coefficient/Electrical Conductivity and Time Domain Thermoreflectance, (n.d.). https://www.netzsch-thermal-analysis.com/en/products-solutions/thermal-diffusivity-conductivity/ (accessed April 26, 2021).

[168] K. G. Prashanth, S. Scudino, T. Maity, J. Das, J. Eckert, Is the energy density a reliable parameter for materials synthesis by selective laser melting?, Mater. Res. Lett. 5 (2017) 386–390. https://doi.org/10.1080/21663831.2017.1299808.

[169] C. Groden, K. D. Traxel, A. Afrouzian, E. Nyberg, A. Bandyopadhyay, “Inconel 718-W7Ni3Fe bimetallic structures using directed energy deposition-based additive manufacturing,” *Virtual and Physical Prototyping*, January 2022. https://doi.org/10.1080/17452759.2022.2025673